

American Journal of Science

DECEMBER 2002

FLOW FOCUSING IN OVERPRESSURED SANDSTONES: THEORY, OBSERVATIONS, AND APPLICATIONS

PETER B. FLEMINGS*, BETH B. STUMP***, THOMAS FINKBEINER*****,
and MARK ZOBACK***

ABSTRACT. Dipping permeable sandstone bodies encased in overpressured low permeability mudstone have a characteristic pressure field: sandstone pressures follow the hydrostatic gradient while mudstone pressures have a steeper (often lithostatic) gradient. This pressure distribution drives fluid into the base of the sandstone and expels it at the crest. We use mudstone pressures predicted from porosity and measured sandstone pressures to describe the spatial variation in pressure in two Eugene Island 330 reservoirs (Gulf of Mexico). In one severely overpressured reservoir, bounding mudstones are less compacted at the reservoir crest than at the reservoir base, and we interpret that flow is focused along the reservoir and expelled at the crest. In the second reservoir, mudstone is compacted around the base of the sandstone, and we interpret pore fluids were drawn into the sandstone. Dipping sandstone bodies encased in overpressured mudstone regulate hydrocarbon migration, affect borehole stability, and impact slope stability.

INTRODUCTION

Sedimentation rate often exceeds the ability of sediments to drain in rapidly formed basins. As a result, pore fluid is overpressured because it supports overlying material and sediment is underconsolidated. Gibson (1958) used a forward model to describe in one dimension the evolution of pressure, porosity, and flow during sedimentation. Bethke (1985) and Harrison and Summa (1991) extended this approach to model the hydrodynamic evolution of sedimentary basins in multiple dimensions. Neuzil (1995) summarized the conceptual viewpoint that overpressure drives hydrodynamic processes in sedimentary basins. These and subsequent studies focused on basin scale (10's to 100's of kilometers) processes, which did not allow analysis of flow and consolidation within and around individual sandstone beds.

Inverse models predict pore fluid pressure from compaction state. The relation between porosity and effective stress is constrained where fluid pressure is known, and then fluid pressure is predicted from porosity in zones where pressure is unknown (Athy, 1930; Rubey and Hubbert, 1959; Hottman and Johnson, 1965; Wallace, 1965; Eaton, 1975; Hart and others, 1995). The approach is generally used to predict pressure in individual wells and the results are seldom integrated with hydrodynamic models.

We use forward and inverse approaches to study pressure, compaction, and flow in overpressured, dipping, sandstone bodies that are encased in mudstone. We extend previous forward modeling by using simple flow models to give physical insight into how sandstone geometry and structural geometry control pressure and flow. We then

*Department of Geosciences, The Pennsylvania State University, University Park, Pennsylvania 16802; flemings@geosc.psu.edu

**Now at ChevronTexaco Production Co., 935 Gravier Street, New Orleans, Louisiana 70112

***Department of Geophysics, Stanford University, Stanford, California 94305-2215

****Now at Geomechanics International, Technologie Zentrum Mainz, IBM-Gelände, Gebäude 51, Hechtsheimer Str. 2, 55131 Mainz, Germany

NOMENCLATURE

Name	Description	Units
a	half-length of sand	L
B	pore pressure build-up coefficient	dimensionless
C_1	constant for overburden geometry	L
C_2	constant for overburden geometry	dimensionless
C_3	constant for sandstone geometry	L
C_4	constant sandstone geometry	dimensionless
d	length scale	L
f	acoustic formation factor	dimensionless
g	gravitational acceleration	L/T ²
h	sand thickness	L
k	intrinsic permeability	L ²
κ	hydraulic diffusivity	L ² /T
K	effective stress ratio	dimensionless
l	length of sand	L
P	water phase fluid pressure	M/LT ²
P^*	fluid overpressure (water-phase)	M/LT ²
P_{ms}^*	mudstone overpressure (water-phase)	M/LT ²
P_{ms}	mudstone pressure (water-phase)	M/LT ²
P_{ss}^*	sandstone overpressure (water-phase)	M/LT ²
P_{ss}	sandstone pressure (water-phase)	M/LT ²
P_g	gas phase pressure	M/LT ²
P_h	hydrostatic pressure	M/LT ²
P_o	oil phase pressure	M/LT ²
P_w	water phase pressure	M/LT ²
r	radius	L
S_{hmin}	minimum horizontal stress	M/LT ²
S_v	overburden (lithostatic) stress	M/LT ²
$SSTVD$	Sub Sea True Vertical Depth	L
t	time	T
u	horizontal velocity	L/T
U	far field flow velocity	L/T
v_z	vertical velocity	L/T
v_x	horizontal velocity	L/T
v	acoustic velocity of formation	L/T
v_m	acoustic velocity of matrix	L/T
V_{ss}	sandstone volume	L ³
x	horizontal position	L
y	horizontal position	L
z	depth	L
β	bulk compressibility	LT ² /M
β_f	fluid compressibility	LT ² /M
μ	dynamic viscosity	M/LT
ϕ	porosity	L ³ /L ³
ϕ_0	reference porosity	L ³ /L ³
θ	angle of rotation	radians

ρ_b	bulk density	M/L ³
ρ_f	fluid density	M/L ³
ρ_w	water density	M/L ³
σ_v	vertical effective stress	M/LT ²
τ	pressure relaxation timescale	T
γ	angle between far field flow and sandstone in steady-flow model	radians
Φ	flow potential	L/T
Ψ	stream function	L/T
η	elliptical coordinate	-
ξ	elliptical coordinate	-

present one of the first attempts to document the spatial variation in mudstone pressures that bound dipping sandstone bodies by mapping consolidation and predicting pressure. Through insights gained in our models, we infer the paleo- pressure evolution of these systems. We close by demonstrating how flow focusing impacts hydrocarbon migration, drilling strategy, and slope stability. The results demonstrate that flow at the scale of individual sandstone beds impacts basin scale flow.

OVERPRESSURE IN SANDSTONES AND MUDSTONES

The equation for flow through a volume element composed of a constant number of solid grains where only Darcy flow and sediment loading are considered is

$$\left(\frac{\beta\phi}{1-\phi} + \phi\beta_f \right) \frac{DP}{Dt} = \frac{1}{\rho_f} \nabla \cdot \left(\frac{k\rho_f}{\mu} \nabla P^* \right) + \frac{\beta\phi}{(1-\phi)} \frac{DS_v}{Dt}. \quad (1)$$

Change in pressure (DP) results from flow in or out of the element and the rate of burial $\left(\frac{DS_v}{Dt} \right)$; DP is proportional to the fluid and bulk compressibilities (β_f, β). k is the permeability, ρ_f is the water density, μ is the dynamic viscosity, and ϕ is porosity. Equation (1) is derived by Gordon and Flemings (1998) who built upon Palciauskas and Domenico's (1989) derivation. We assume that solid grains are incompressible, β_f and β are compressible ($d\rho_f/\rho_f = \beta_f dP$; $d\phi = -\beta\phi\sigma_v$), and strain is uniaxial. We simplify equation (1) to consider undrained behavior and steady flow within an overpressured dipping sandstone body that is surrounded by mudstone.

Undrained Behavior

If the mudstone is undrained, equation (1) reduces to,

$$DP_{ms} = BDS_v. \quad (2)$$

The change in mudstone pressure (DP_{ms}) is proportional to the change in the overburden stress ($DS_v = \rho_b g dz$). The pore pressure build-up coefficient $\left(B = \frac{B}{B + B_f(1-\phi)} \right)$, defines the proportion of the change in total vertical stress that is supported by the fluid. When the bulk compressibility is much greater than the fluid compressibility ($\beta \gg \beta_f$), $DP = DS_v$ whereas when ($\beta \ll \beta_f$), $DP = 0$, and the rock bears all of the increase in load. In underconsolidated mudstones from the Gulf of Mexico, ($\beta \gg \beta_f$) and $B = \sim 1.0$ (appendix). Biot (1941), Skempton (1954), Rice and Cleary (1976), Van der Kamp and Gale (1983), Green and Wang (1986), and Wang and Davis (1996) explored the behavior of B .

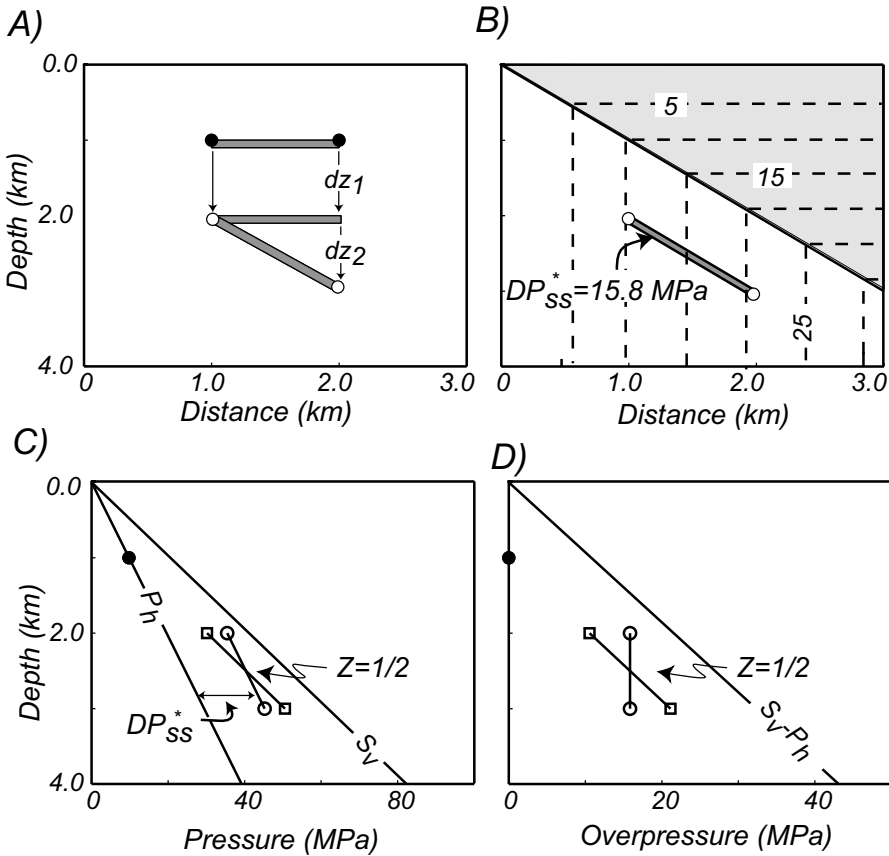


Fig. 1. Undrained model. (A) A hydrostatically pressured sandstone body (grey-shaded lens) is initially encased in mudstone at 1 km depth. Its left edge is buried to 2 km and its right edge is buried to 3 km. (B) Sediment loading (shaded area) increases the sandstone overpressure (DP_{ss}^*) to 15.8 MPa. Contours (dashed lines) are mudstone overpressure. (C) Sandstone pressure (circles) parallels the hydrostatic gradient and is elevated above hydrostatic by DP_{ss}^* . Mudstone pressure follows the lithostatic pressure gradient (squares). Sandstone pressure before burial is hydrostatic (open circle at 1 km depth). Z is 1/2 because the sandstone pressure equals the mudstone pressure at one half of the sandstone relief. Hydrostatic pressure (P_h) and the lithostatic stress (S_v) are shown ($\frac{dP_h}{dz} = 10.5 \text{ MPa/km}$, $\frac{dS_v}{dz} = 21.0 \text{ MPa/km}$). (D) Sandstone overpressure DP_{ss}^* is constant (circles). Solid circle at 1 km depth records no overpressure before burial.

We consider the pressure distribution that results from rapid burial of a sandstone. A horizontal, hydrostatically-pressured, sandstone body of constant thickness is buried a depth dz_1 and then rotated such that one edge is buried a further increment dz_2 (fig. 1A). The change in sandstone overpressure (DP_{ss}^*) is,

$$DP_{ss}^* = B(\rho_b - \rho_f)g \left(dz_1 + \frac{dz_2}{2} \right). \quad (3)$$

Equation (3) is derived in the appendix. The change in mudstone pressure (DP_{ms}) equals the increase in overburden stress (eq 1) (fig. 1B, C and D). The sandstone pressure follows the hydrostatic gradient but increases by DP_{ss}^* (fig. 1B and C).

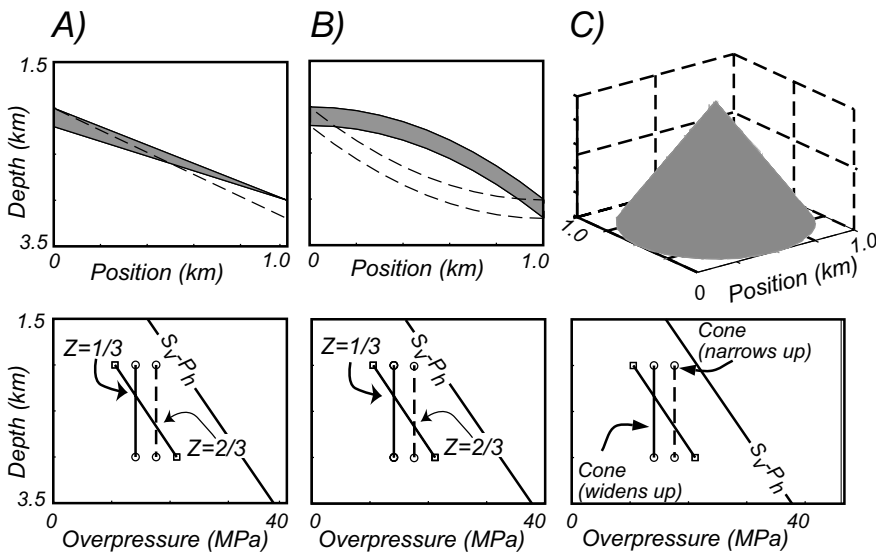


Fig. 2. Overpressure for different sandstone geometries in undrained model. (A) When sandstone thickens down-dip (dashed line), overpressures are elevated relative to when sandstone thickens up-dip (solid line). (B) Synclinal geometry (dashed line) increases sandstone overpressures relative to anticlinal geometry (solid line). (C) A three-dimensional, cone-shaped, anticlinal structure (dashed line) elevates sandstone overpressure whereas a three-dimensional synclinal geometry reduces sandstone overpressure (solid line). Results derived in appendix.

We introduce the parameter Z , the dimensionless depth along structure where the sandstone and mudstone pressure are equal. It is calculated by dividing the vertical distance from the crest to where the sandstone and mudstone pressures are equal by the total relief of the sandstone. Above Z , the sandstone pressure exceeds the mudstone pressure; below Z , the sandstone pressure is less than the mudstone pressure. In this example (fig. 1C), $Z = 1/2$: the sandstone pressure equals the mudstone pressure at the structural midpoint of the sandstone (fig. 1C and D). Z quantifies the magnitude of sandstone pressure. Higher Z values equate to a larger difference in pressure between the sandstone and mudstone at the crest.

DP_{ss}^* (and hence Z) is controlled by the sandstone geometry and the load geometry (appendix). If the sandstone body thins toward the crest, its pore pressure is elevated ($Z = 2/3$) relative to the case where it thickens toward the crest ($Z = 1/3$) (fig. 2A). If the loading generates a synclinal geometry, P_{ss}^* is greater ($Z = 2/3$) than for the case of an anticlinal geometry ($Z = 1/3$) (fig. 2B). Finally, we compare a planar geometry (fig. 2) with a cone-shaped geometry (fig. 3C). When the cone narrows upward (dome-shaped), P_{ss}^* is elevated ($Z = 2/3$) relative to when it narrows downward (bowl-shaped) ($Z = 1/3$).

Steady Flow

If flow is steady and mudstone properties are homogenous and isotropic, equation (1) simplifies to Laplace's equation:

$$\nabla^2 P^* = 0. \quad (4)$$

Phillips (1991) solved equation (4) analytically for a thin straight permeable body encased in low permeability material (appendix). He assumed that the body is long relative to its width, that its permeability is much greater than the surrounding

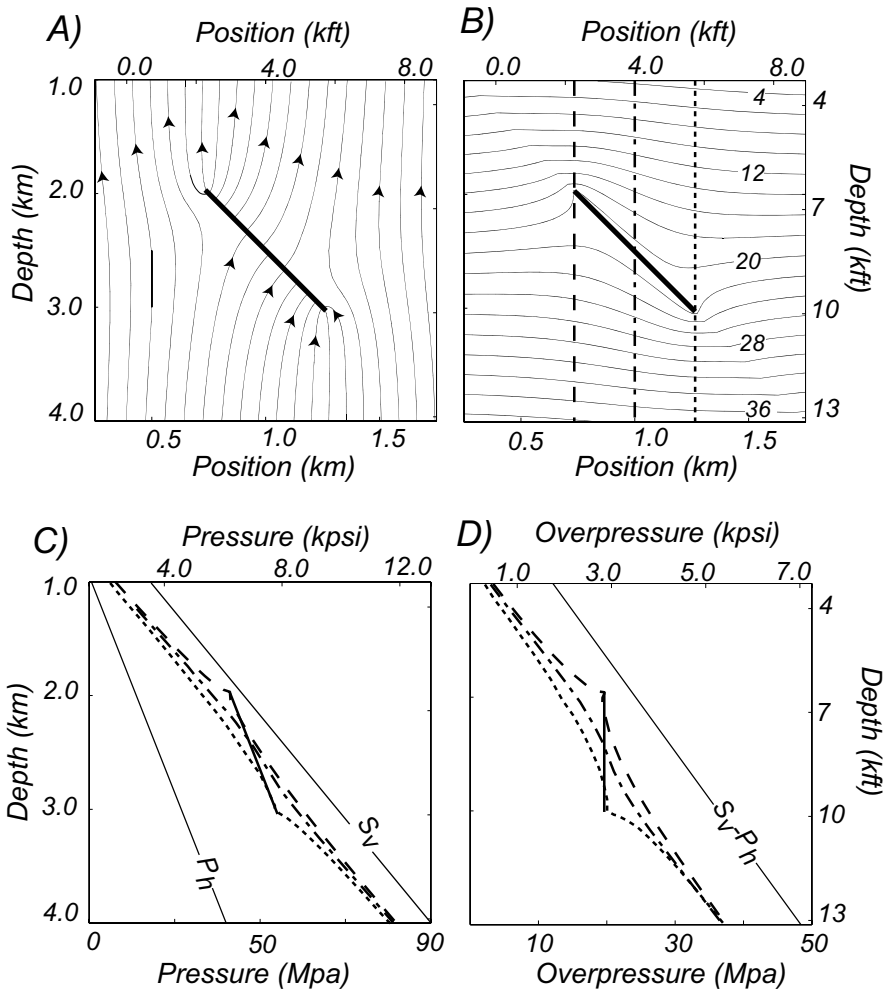


Fig. 3. Steady-flow model. (A) Streamlines record primarily vertical flow, with enhanced flow into the base of the sandstone and out of its crest. (B) Mudstone overpressure contours (MPa) are elevated at the sandstone's crest and are depressed near its base. Vertical lines locate pressure profiles shown in C and D. (C) Mudstone pressures converge onto the sandstone pressure at the crest (long dashes), center (dash-dots) and base (dots) of the sandstone body. (D) Overpressure in sandstone is constant, overpressure in mudstone rises to meet the pressure at the crest of the sandstone. The far field mudstone pressure gradient is $\frac{dS_v}{dz} = 21.0 \text{ MPa/km}$.

material, and that flow is steady and unidirectional far from the permeable body. We use this solution to examine flow through a dipping overpressured sandstone body (fig. 3). We assume the pressure gradient far from the sandstone equals the lithostatic gradient, which satisfies Phillips' far-field boundary condition for constant rock and fluid properties $\left(v_z = -\frac{k}{\mu} \frac{dP^*}{dz}, v_x = -\frac{k}{\mu} \frac{dP^*}{dx} = 0 \right)$.

In the model, flow is focused into the sandstone at its base and out of the sandstone at its crest (fig. 3A). At the base of the sandstone, overpressure contours are depressed and at the crest they are elevated (fig. 3B). Pressure within the sandstone

follows the hydrostatic gradient (fig. 3C and D) and (Z) is 1/2. The mudstone pressure gradient along a vertical profile that penetrates the midpoint of the sandstone is constant and equal to the far-field pressure gradient (dash-dot line, fig. 3). At its crest (dashed line), the sandstone pressure is greater than the adjacent mudstone pressure (fig. 3C). In a vertical profile through the sandstone crest, the mudstone pressure (dashed line) rises above the far-field pressure (dash-dot line) to equal sandstone pressure (fig. 3C); beneath the sandstone, the mudstone pressure returns to the far-field pressure. Just beneath the crest, the mudstone overpressure decreases with depth, which records downward flow (fig. 3D). At the structural lowpoint (dotted line), the mudstone pressure drops below the far-field pressure (dash-dot line) in order to converge on the sandstone pressure. Beneath the sandstone, the pressure rises toward the far-field pressure (fig. 3C).

Model Discussion

If the loading rate $\left(\frac{DS_v}{Dt}\right)$ is rapid relative to the rate that pressure is diffused, the undrained model describes the system, whereas if the loading rate is slow, the steady-flow model is a more appropriate description. The models are extreme examples of pressure distributions that can result, yet they have many similarities. In both models, the sandstone pressure gradient is hydrostatic while the mudstone pressure gradient far from the sandstone is lithostatic. In both models, geometry controls sandstone overpressure. However, in the undrained model, there are pressure discontinuities at the mudstone-sandstone interface, whereas in the steady-flow model pressures are continuous over the sandstone to the mudstone.

The pressure discontinuities predicted by the undrained model will dissipate with time. The timescale for a pressure pulse (τ) to propagate through a uniform medium is

$$\tau = \frac{d^2}{2\kappa}, \quad (5)$$

where κ is the hydraulic diffusivity and d is the length scale (Phillips, 1991). For equation (1),

$$\kappa = \frac{k}{\mu \left(\frac{\phi\beta}{1-\phi} + \phi\beta_f \right)}. \quad (6)$$

The permeability of Eugene Island mudstones is $3 \times 10^{-16} \text{ m}^2$ (Stump and Flemings, 2002). As a result, a pressure disturbance will dissipate over a 1000 meter length scale in only 700 years ($\beta = 3.1 \times 10^{-2} \text{ MPA}^{-1}$, $\phi = .3$, $\mu = .001 \text{ kg/ms}$, $\beta_f = 4.8 \times 10^{-4} \text{ MPA}^{-1}$). Thus, in geologic structures that form over 10,000 to 100,000 years, abrupt pressure discontinuities will not be present. Neuzil (1994) suggested mudstone permeability ranges from 10^{-21} m^2 to 10^{-16} m^2 for a porosity of 30 percent. The lower permeability values generate much longer dissipation times (eqs 5 and 6).

Dickinson (1953) and Rubey and Hubbert (1959) recognized that in overpressured strata, the pressure gradient is less in permeable sandstones than in the bounding low permeability mudstone, and England and others (1987), Mann and Mackenzie (1990), and Yardley and Swarbrick (2000) suggested that under these conditions focused flow results. Our contribution is to use two-dimensional models to give physical insight into how sandstone pressure and mudstone pressure are controlled by stratigraphic and structural geometry, to describe the associated flow field, and provide a conceptual framework to examine field data. Iliffe and others (1999) also illustrated how pressures are amplified by sandstone geometry.

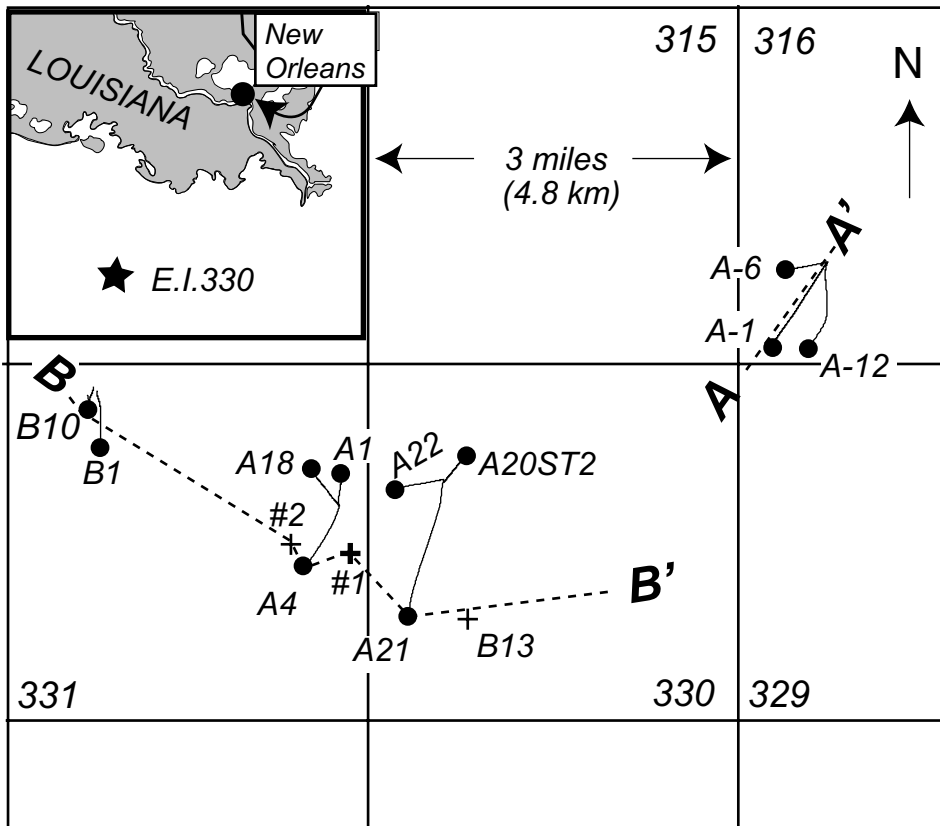


Fig. 4. The E.I. 330 field is in the Gulf of Mexico, 272 km (169 mi) southwest of New Orleans, LA, U.S.A. in a water depth of 77 m. Plus symbols record vertical boreholes; solid lines record deviated well paths; filled circles show bottom-hole locations of deviated wells. Cross-section locations A-A' (fig. 10), and B-B' (fig. 13) are shown.

FLOW FOCUSING IN THE EUGENE ISLAND 330 FIELD

We examine the Lentic-1 and the OI-1 reservoirs of the Eugene Island 330 (E.I. 330) field. This field is located within a salt-withdrawal, Plio-Pleistocene mini-basin (fig. 4) that is bounded to the north and northwest by a large regional growth fault. The Lentic-1 is the deepest and most overpressured reservoir in the field, and the overlying OI-1 is moderately pressured. Holland and others (1990), Alexander and Flemings (1995) and Rowan and others (1998) describe the stratigraphic and structural architecture of this region.

Methodology of Pressure Analysis

We used pre-production pressures derived from Repeat Formation Tests (RFT's) and shut-in bottom hole pressure surveys to determine sandstone pore pressure (table 1). In reservoirs, the gas- or oil-phase pressures (P_g , P_o) exceed the water pressure (P_{ss}), due to the differences in fluid density. We calculate P_{ss} for each reservoir by assuming that the water pressure equals the hydrocarbon pressure at the hydrocarbon-water contact (table 2).

In low permeability rocks, pressure is occasionally measured directly with a probe (Schultheiss and McPhail, 1986; Urgeles and others, 2000; Ostermeier and others,

TABLE 1
Reservoir Pressure Measurements

Reservoir Sandstone	Fault Block	Well	SSTVD (MPa)	P (MPa)	S _v (MPa)	Oil Gradient (MPa/km)	Gas Gradient (MPa/km)
Lentic-1	FB-C	316 A-4	2113.1	39.07	43.90	6.79	n/a
Lentic-1	FB-C	316 A-8	2029.0	39.2	42.15	6.79	n/a
OI-1	FB-B	330 B-14	2147.3	36.43	44.98	5.66	2.26
OI-1	FB-C	330 A-3	2294.8	36.64	47.58	7.24	2.26

2001; Whittle and others, 2001) or by long-term monitoring (Neuzil, 1993; Becker and others, 1997). However, the most common method is to use an empirical relationship between porosity and effective stress to predict pressure. Terzaghi (1943) defined porosity of soils as a function of vertical effective stress. Rubey and Hubbert (1959) and Palciauskas and Domenico (1989) expanded this work and applied it to geologic problems. This approach is applied to core data (Boatman, 1967), wireline logs (Hottman and Johnson, 1965; MacGregor, 1965; Ham, 1966; Hart and others, 1995; Moore and others, 1995; Moore and Tobin, 1997), or seismic data (Pennebaker, 1968; Weakley, 1989). The success of the method depends on its ability to measure porosity and the validity of the porosity-effective stress relationship assumed.

We assume porosity (ϕ is proportional to vertical effective stress (σ_v):

$$\phi = \phi_0 e^{-\beta \sigma_v} \quad (7)$$

ϕ is a reference porosity, σ_v is the vertical effective stress ($\sigma_v = S_v - \rho_w g z - P_{ms}^*$), S_v is the overburden stress, ρ_w is the water density, g is the acceleration due to gravity, z is the depth below sea surface, and P_{ms}^* is the mudstone overpressure. ϕ is calculated from velocity with an empirical relationship (eq 8) developed by Raymer and others (1980) and enhanced by Raiga-Clemenceau and others (1986):

$$\phi = 1 - \left(\frac{v}{v_m} \right)^{1/f} \quad (8)$$

v is the bulk velocity of the formation. Issler (1992) found that the matrix velocity (v_m) is 4545 m/s and the acoustic formation factor (f) is 2.19 for non-calcareous, low total organic carbon mudstone. Stump and Flemings (2002) also found $f = 2.19$ in core samples from the E.I. 330 field. We apply equations (7) and (8) only to mudstones,

TABLE 2
Reservoir Fluid Contacts

Reservoir Sand	Fault Block	Top of structure, SSTVD (m)	Oil-water contact, SSTVD (m)	Gas-oil contact, SSTVD (m)	Oil column (m)	Gas column (m)
Lentic-1	FB-C	1936.0	2132.0	n/a	165.9	n/a
OI-1	FB-B	2048.8	2689.3	2628.7	60.7	387.8
OI-1	FB-C	2240.9	2689.3	2628.7	60.7	387.8

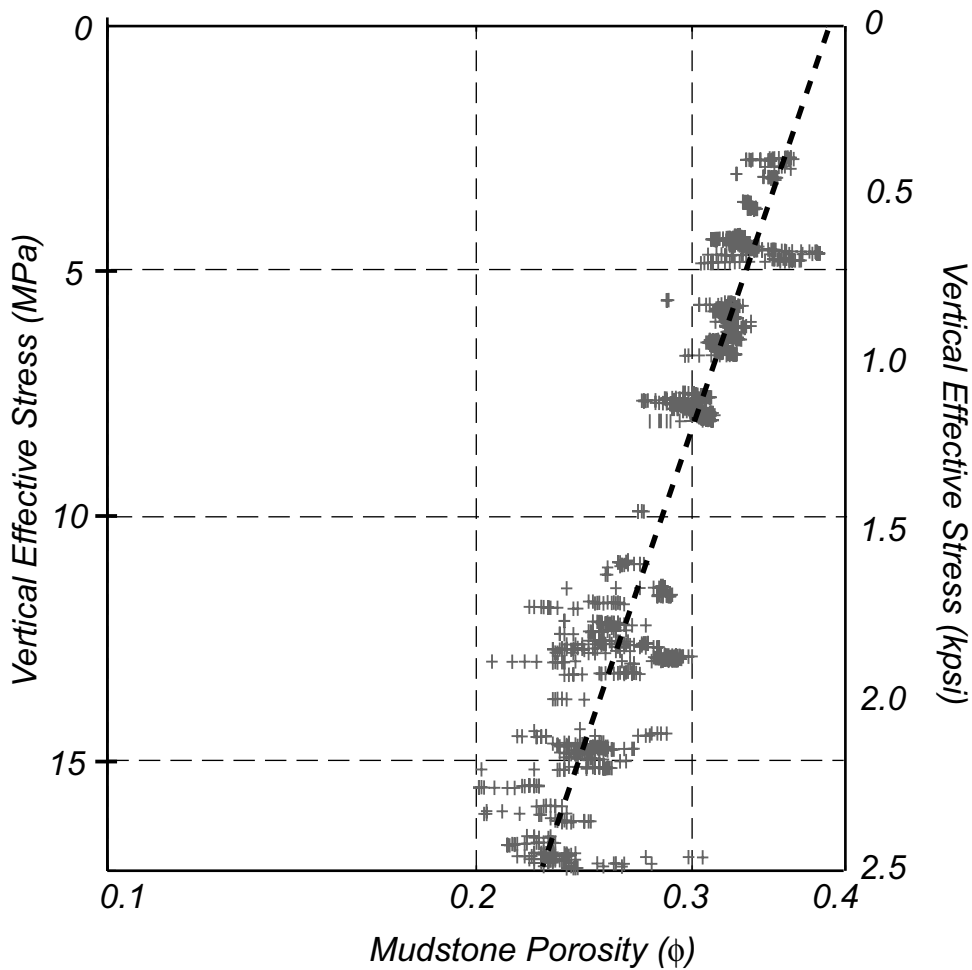


Fig. 5. Mudstone porosity (ϕ) versus vertical effective stress (σ_v) between the seafloor and 1500 meters depth in the 331 #1 well (located in fig. 4). In this zone, pressures are assumed to be hydrostatic, which allows effective stress to be calculated ($\sigma_v = S_v - P_h$). Dashed line is a log-linear regression with slope $\frac{1}{\beta} = \frac{1}{3.13 \times 10^{-2} \text{MPa}^{-1}}$.

which are distinguished by their high gamma ray values in the wireline log. These mudstones are unlithified, contain approximately 40 percent quartz, 40 to 50 percent clay (primarily smectite and illite with lesser amounts of kaolinite and chlorite), and less than 10 percent plagioclase and potassium feldspar. They are composed of 80 percent silt- and clay-sized particles and 20 percent very fine-grained sand (Stump and Flemings, 2002).

The reference porosity (ϕ_0) and the compressibility (β) (eq 7) are estimated from the change in porosity versus depth in the shallow section of the 331#1 well where the pressures are assumed to be hydrostatic (fig. 5). The lithostatic stress (S_v) is calculated by integrating the wireline bulk density log (Finkbeiner and others, 1996). The parameters used for each calculation are shown in table 3. Once ϕ_0 and β are constrained, equation (7) is re-arranged to predict overpressure from porosity:

TABLE 3
Mudstone Pressure Estimates

Well	Fault Block	SSTVD (m)	f (-)	v (m/s)	v_m (m/s)	ϕ (%)	ϕ_0 (%)	β (MPa ⁻¹)	S_v (MPa)	P_{ms} (MPa ⁻¹)
316 A-1	Lentic-1	2000.6	2.19	2313.6	4902	29.0	38.6	3.683×10^{-2}	41.44	33.66
316 A-6	Lentic-1	2132.9	2.19	2343.0	4902	28.6	38.6	3.683×10^{-2}	44.29	36.12
316 A-12	Lentic-1	2034.5	2.19	2220.7	4902	30.3	38.6	3.683×10^{-2}	47.44	35.79
331 #1	B	2530.8	2.19	2798.2	4902	22.5	38.6	3.132×10^{-2}	53.46	36.28
331 A-4	B	2644.2	2.19	2713.0	4902	23.6	38.6	3.132×10^{-2}	55.9	40.23
331 #1	B	1951.5	2.19	2634.6	4902	24.6	38.6	3.132×10^{-2}	40.39	26.07
330 A-22	B	1969.5	2.19	2872.2	4902	21.6	38.6	3.132×10^{-2}	40.78	25.03

$$P_{ms}^* = \frac{1}{\beta} \ln\left(\frac{\phi}{\phi_0}\right) + S_v - \rho_w g z. \quad (9)$$

P_{ms}^* is the mudstone overpressure predicted from porosity. We discuss below why P_{ms}^* is a lower-bound estimate of the *in-situ* overpressure. Hart and others (1995), Gordon and Flemings (1998) and Dugan and Flemings (2000) presented details of this approach.

P_{ms} is predicted for two wells, one on the upthrown and one on the downthrown side of the regional growth fault in EI-330 (fig. 6). In both wells, velocity increases with depth to the JD horizon. Beneath the JD horizon, the velocity is constant in the 331#1 well (fig. 6A), whereas it decreases with depth in the 316-A1 well (fig. 6B). Above the JD horizon, P_{ms} is hydrostatic. This is necessarily the case for the 330#1 well (fig. 6A) because in this zone we constrained ϕ_0 and β by assuming that pore pressure was hydrostatic (fig. 5). Beneath the JD horizon, P_{ms} reaches 70 percent of the overburden stress at the OI-1, and 90 percent of the overburden stress at the Lentic-1 (fig. 6). At this scale, P_{ms} approximately equals both the measured reservoir pressures (circles) and the pressures generated by the high density muds used during drilling (dashed line) (fig. 6A and B). In the ensuing section, we focus on the Lentic-1 and OI-1 reservoirs and compare P_{ms} with P_{ss} , the reservoir pressure.

Lentic-1 reservoir.—The Lentic-1 is produced on the upthrown side of the regional growth fault in Blocks 330 and 316 (fig. 7). We analyze the 316-A1 well, which is near the crest, and the 316-A6 well, which is lower on the structure (fig. 7). In the 316-A1, the mudstone velocity decreases and porosity increases from 1980 to 2000 meters (fig. 8A). In this zone, which is above the sandstone, the mudstone pressure gradient $\left(\frac{dP_{ms}}{dz}\right)$ is greater than the lithostatic gradient. Beneath the Lentic-1, mudstone velocity and porosity are approximately constant and $\left(\frac{dP_{ms}}{dz}\right)$ is less than the lithostatic gradient (fig. 8A). In the 316-A6, above the Lentic-1, velocity declines with depth and porosity increases at a slower rate than in the 316-A1 well (fig. 8B). As a result, $\left(\frac{dP_{ms}}{dz}\right)$ above the sandstone is lower at the 316-A6 than at the 316-A1 well. Beneath the Lentic-1, velocity and porosity are approximately constant and P_{ms} rises slightly with depth in both wells.

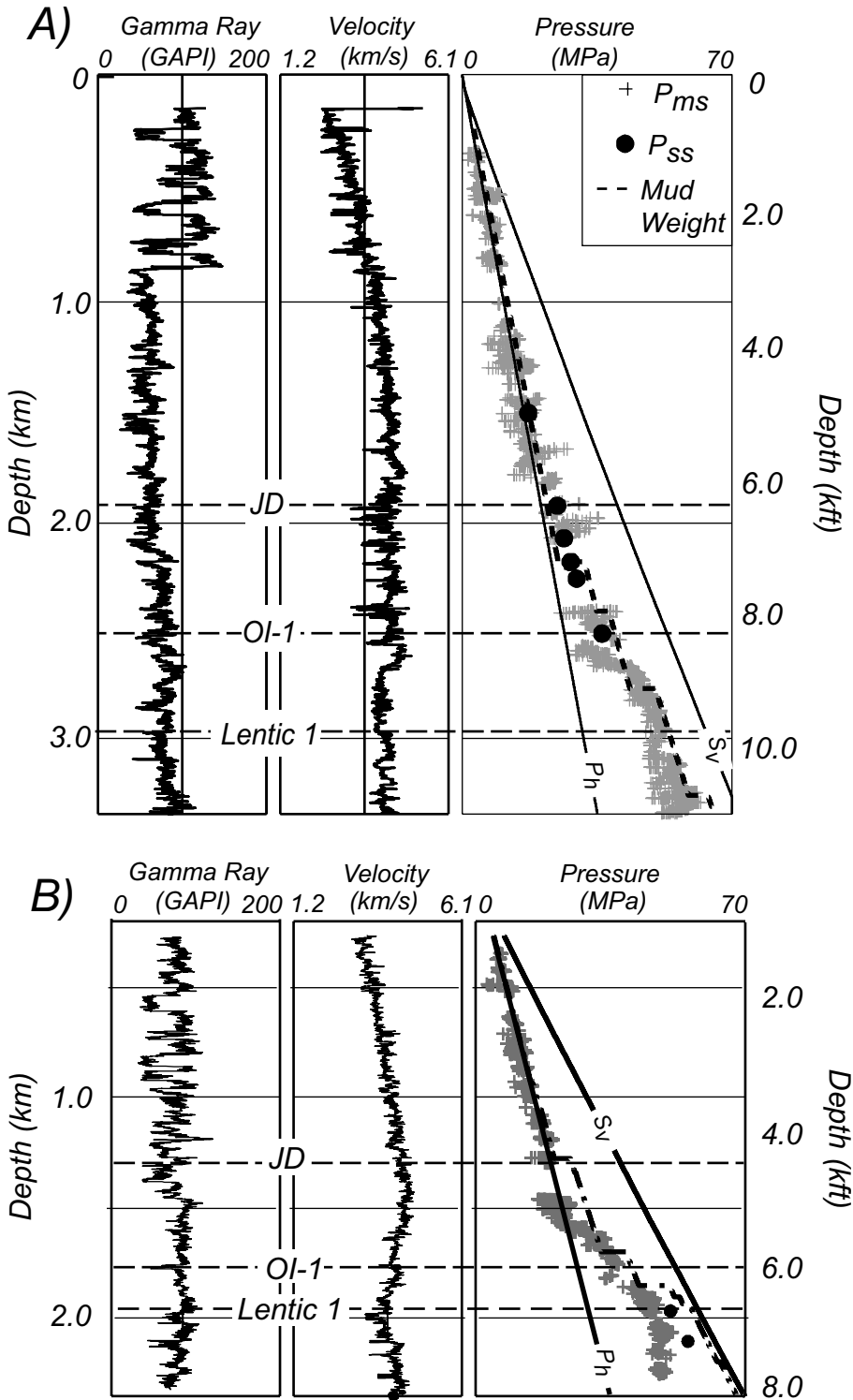


Fig. 6. Lithology (Gamma Ray), acoustic velocity, and pore pressure for (A) the 331#1 well and (B) the 316-A1 well. Pressures calculated from 1) drilling mud density (dashed line), 2) mudstone porosity (P_{ms}) (pluses), and 3) reservoir pressures (P_{ss}) (solid circles) are shown. Wells located in figure 4. Depth where wells penetrated the JD, OI-1 and Lentic-1 reservoirs are identified.

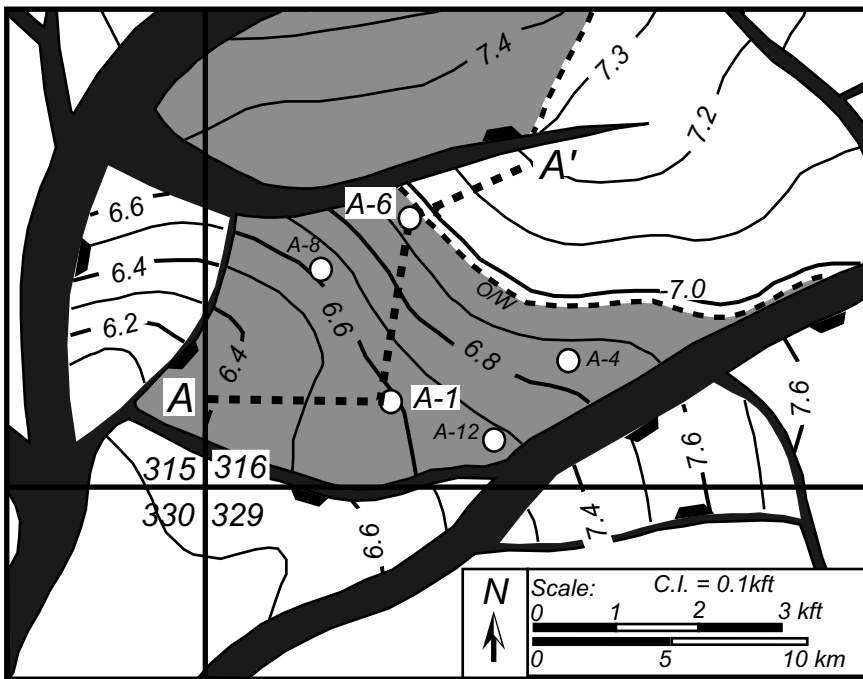


Fig. 7. Structure map of the Lentic-1 reservoir. Depth contours are in kilo-feet SSTVD (1 km = 3.280 kilo-feet). Well penetrations of the Lentic-1 are shown with circles. Thick dashed lines display fluid contacts (O/W: oil-water); oil shown in gray. Structure map was generated by Pennzoil based on 3D seismic data and wireline log data. The faults are vertical projections of the fault plane onto the Lentic-1 horizon; the downthrown side of the fault is marked by black ticks. (Modified from Finkbeiner and others, 2001.)

In three locations where wells penetrate the Lentic-1, P_{ms} (black circles) is less than the water pressure in the underlying sandstone (P_{ss}), and at the crest, P_{ss} is 4.2 MPa greater than P_{ms} (fig. 9). Z could not be determined because it was not possible to image the base of the Lentic-1 with available data. Above the reservoir, porosity contours parallel the sandstone body (fig. 10). Thus, at equivalent depths, the mudstone is less compacted near the crest of the structure. Beneath the Lentic-1, porosity is approximately constant (fig. 10). Above the sandstone, overpressure contours parallel the sandstone body, are closely spaced, and converge toward the crest (fig. 10B). Beneath the sandstone, the overpressure contours are widely spaced (fig. 10B).

The overpressure field is similar to that predicted by the steady-flow model for the crest of the sandstone (fig. 3B). However, P_{ss} is greater than P_{ms} at the sandstone-mudstone interface throughout the cross-section. In the following section we discuss possible reasons for this behavior.

OI-1 reservoir.—The OI-1 reservoir has five fault blocks that contain three reservoirs (fig. 11). Fault Blocks B and C trap a 518 meter (~1700 foot) gas column and a 30 meter (~100 foot) oil column, have identical fluid contacts and identical pressures. Fault Blocks D and E form a second reservoir that traps a 123 meter (~400 foot) oil column. Fault Block A forms a third reservoir with a 152 meter (~500 foot) oil column.

In Fault Blocks B and C, P_{ss} exceeds P_{ms} (black circles) above 2500 meters (~8200 foot) and $P_{ss} < P_{ms}$ below that depth (fig. 12). Z is approximately 1/2. The mudstone pressure immediately above the OI-1 follows the lithostatic gradient (fig. 12). At the

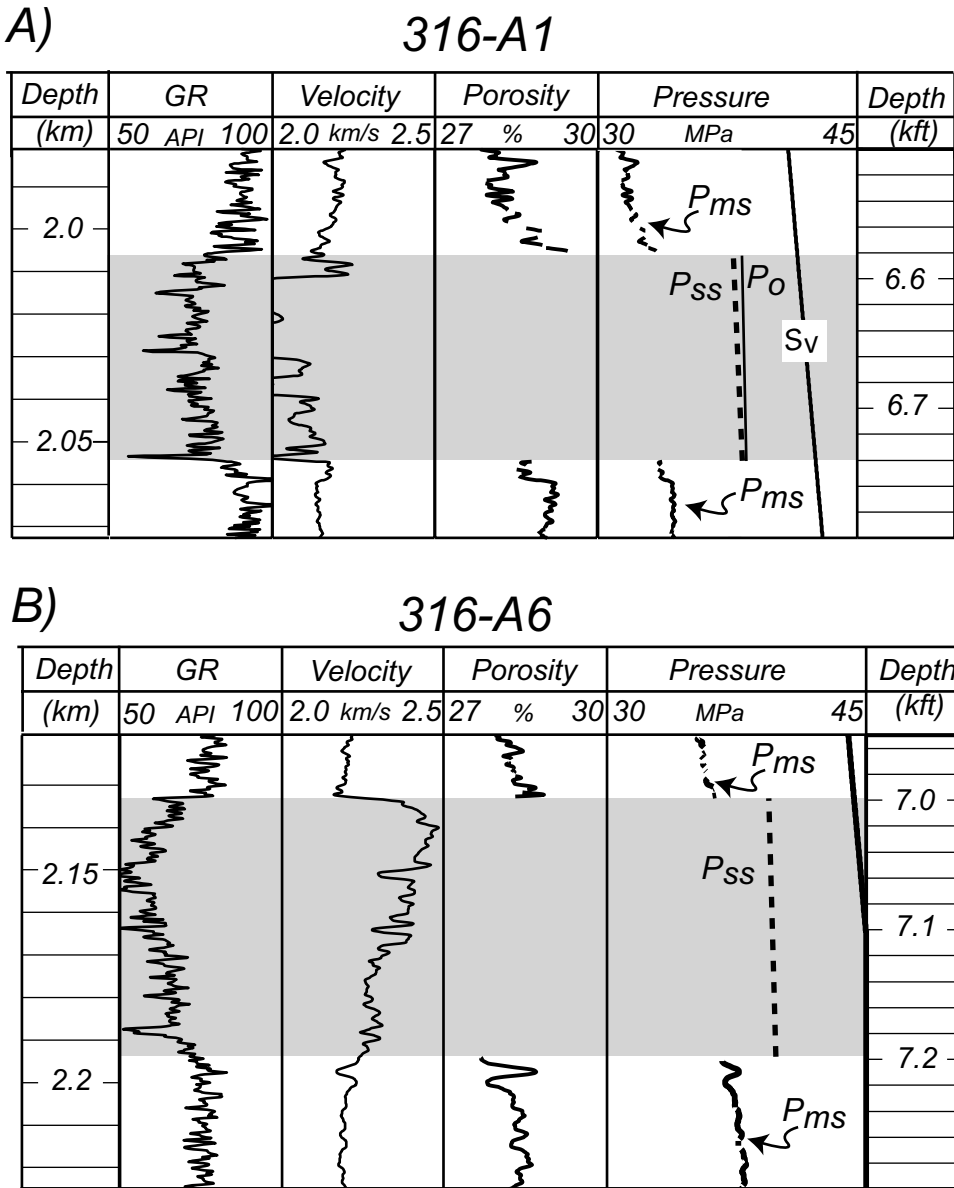


Fig. 8. Petrophysical properties and pressures at two Lentic-1 well penetrations. (A) The 316-A1 is near the reservoir crest (fig. 7). (B) The 316-A6 is lower on the structure and penetrates the Lentic-1 below the oil-water contact (fig. 7). The sandstone (shaded) has low GR (Gamma Ray) values. Porosity is calculated from equation (8); P_{ms} is calculated from equation (9). The oil phase pressure (P_o) and the water phase (P_{ss}) are shown.

crest, the gas phase pressure (P_g) is 5 MPa greater than the water pressure (P_{ss}), because of the buoyant effect of the 518 meter gas column. P_{ms}^* contours above the OI-1 are widely separated, approximately horizontal, and they converge and rise slightly toward the crest of the OI-1 (fig. 13). Beneath the OI-1, overpressure contours

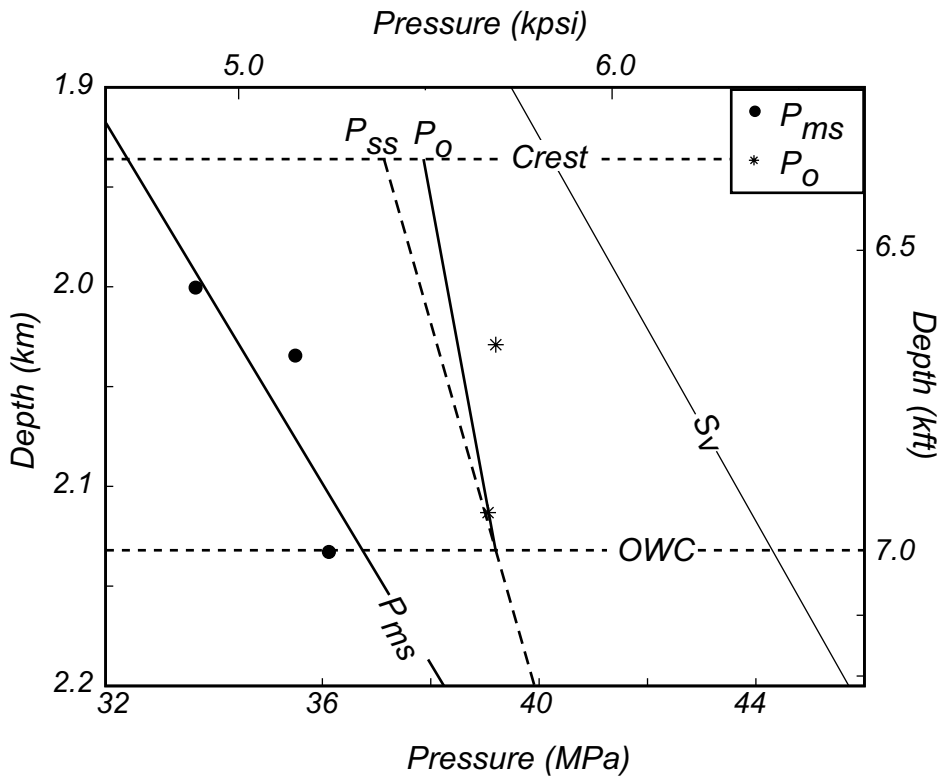


Fig. 9. Pressure-depth plot for the Lentic-1 reservoir. Black circles record porosity-predicted mudstone pressures (P_{ms}) immediately above the Lentic-1 at three different penetrations (table 3). Mudstone pressure line (P_{ms}) is a linear regression of the predicted mudstone pressure values (circles) (table 3). The water phase pressure (P_w) and the oil phase pressure (P_o) are greater than P_{ms} at each location. Reservoir pressures are calculated by extrapolating known pressure gradients (table 1) from measured values (stars).

are closely spaced and they parallel the reservoir; the contours are more closely spaced as the reservoir is approached (fig. 13).

Because P_{ms}^* contours parallel the overlying OI-1 and because these contours record a rapid decrease in pressure as the reservoir is approached, we infer the mudstones beneath the OI-1 drained upward into the OI-1. Several observations complicate this interpretation. First, beneath the OI-1, P_{ss}^* is everywhere higher than the underlying mudstone ($P_{ss}^* = 9.8$ MPa whereas $P_{ms}^* = 6.9$ MPa). Second, P_{ms}^* is greater above the OI-1 than below it. For example, at the B-10 well, P_{ms}^* above the OI-1 is 4.82 MPa greater than P_{ms}^* immediately underlying it (fig. 13).

DISCUSSION

Evolution of Pressure and Stress During Burial

During virgin consolidation, mudstone deforms elasto-plastically and the majority of compaction is irrecoverable. If effective stress decreases, the porosity will recover only the elastic portion of the original deformation. This effect is termed hysteresis or unloading; when it occurs, rocks are over-consolidated, and the porosity-effective stress relationship determined from virgin consolidation will not accurately map the effective stress (Crawford, 1986; Karig and Hou, 1992; Pestana and Whittle, 1999).

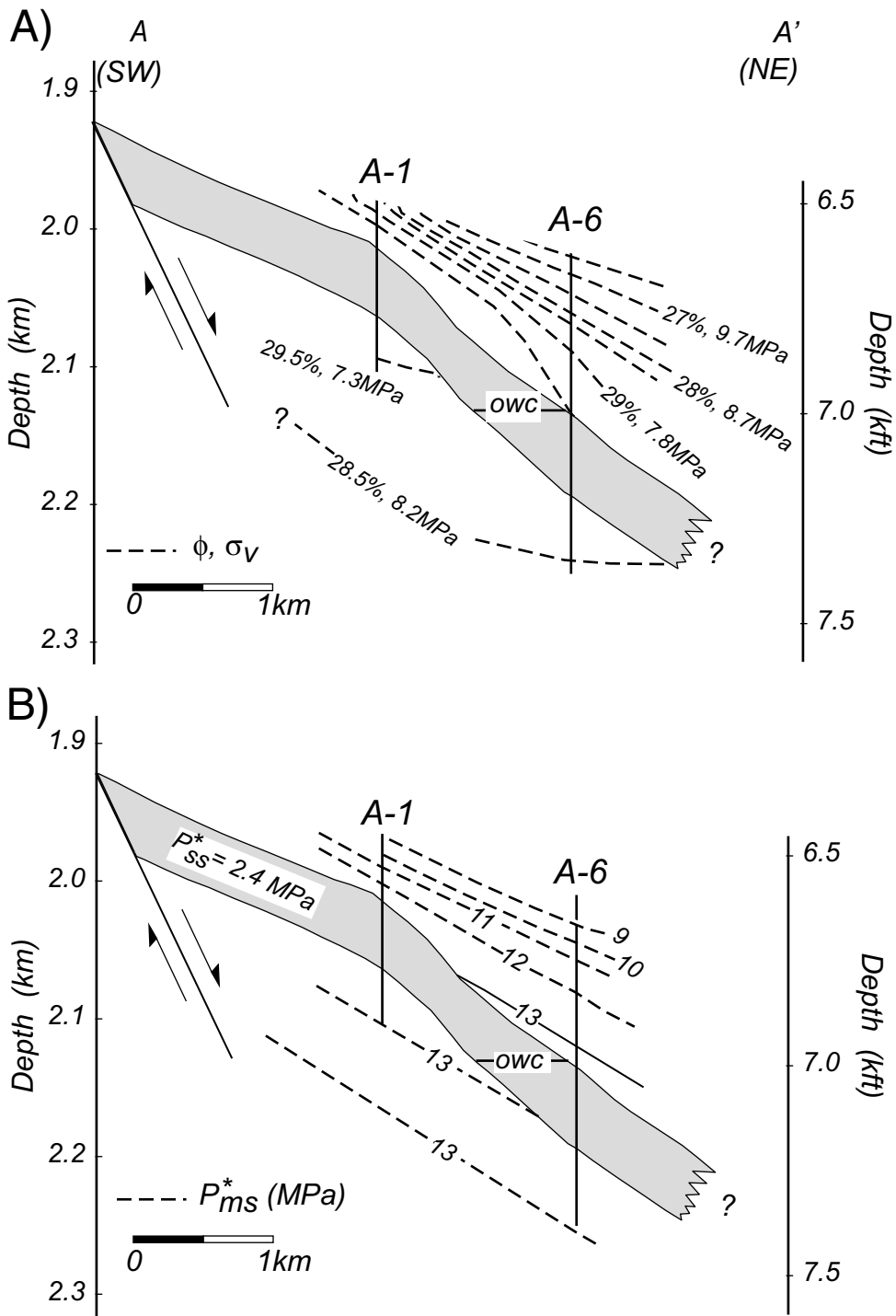


Fig. 10. (A) Contour map of mudstone porosity (ϕ) and the interpreted vertical effective stress (σ_v). Above the reservoir, mudstone porosity contours (interpreted from velocity (eq 8) in the 316-A1 and 316-A6 wells) parallel the reservoir; below the reservoir, porosity is nearly constant. (B) Above the reservoir, mudstone overpressure (P_{ms}^*) contours (from porosity (eq 9)) parallel the reservoir and converge toward the crest. Sandstone pressure from table 1. OWC identifies the oil-water contact shown. A-A' is located in figure 8.

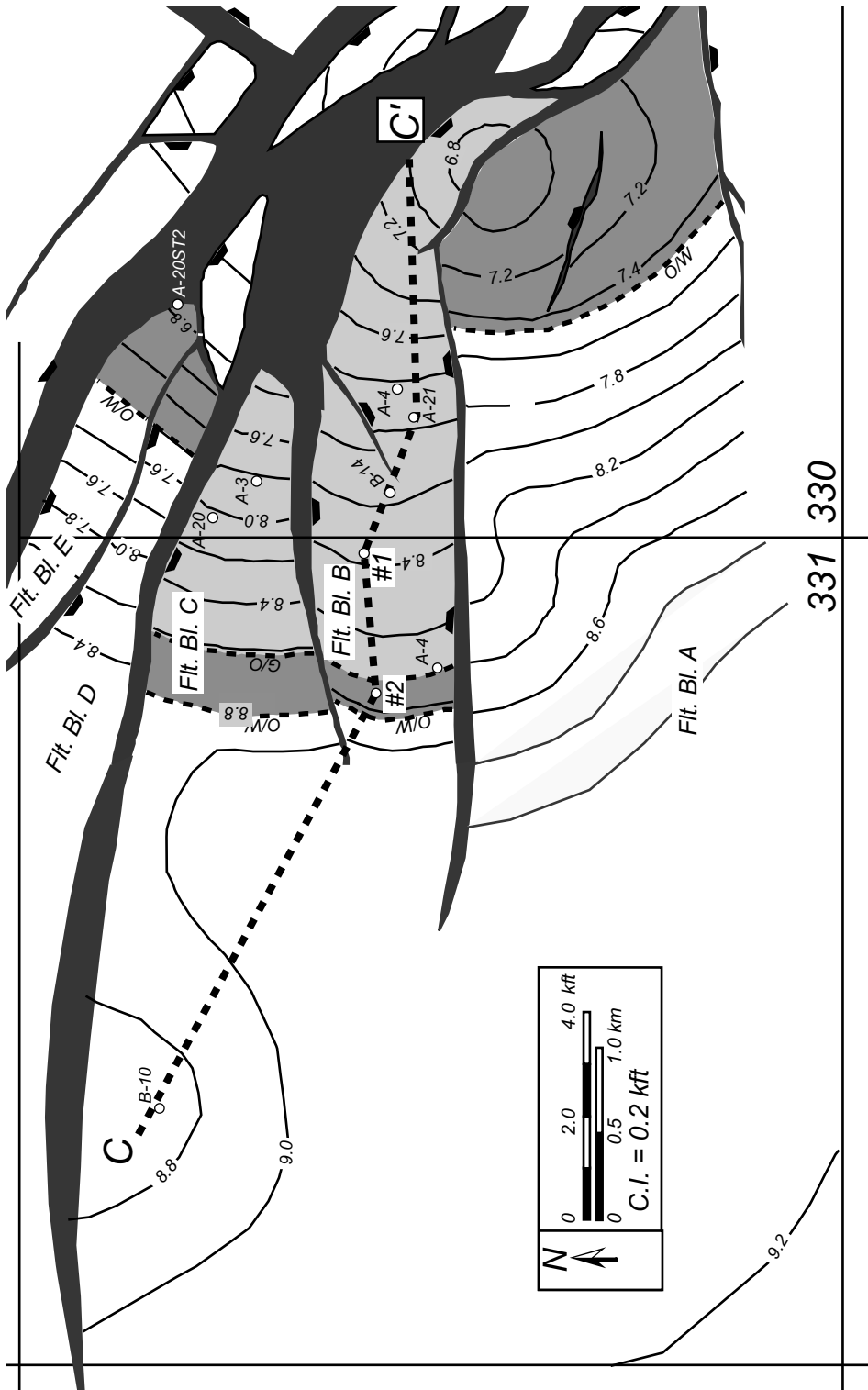


Fig. 11. Structure map of the OI-I sandstone. Depth contours are in kilo-feet (SSTVD) (1 km = 3.28 kilo-feet). Reservoir penetrations marked with circles. Oil-water (O/W) and gas-water (G/W) fluid contacts are labeled for each fault block. The depth intervals filled with oil and gas are shown in dark and light gray. This map integrates Pennzoil's EL-330 map with regional work by Alexander and Flenings (1995) and Rowan and others (1998).

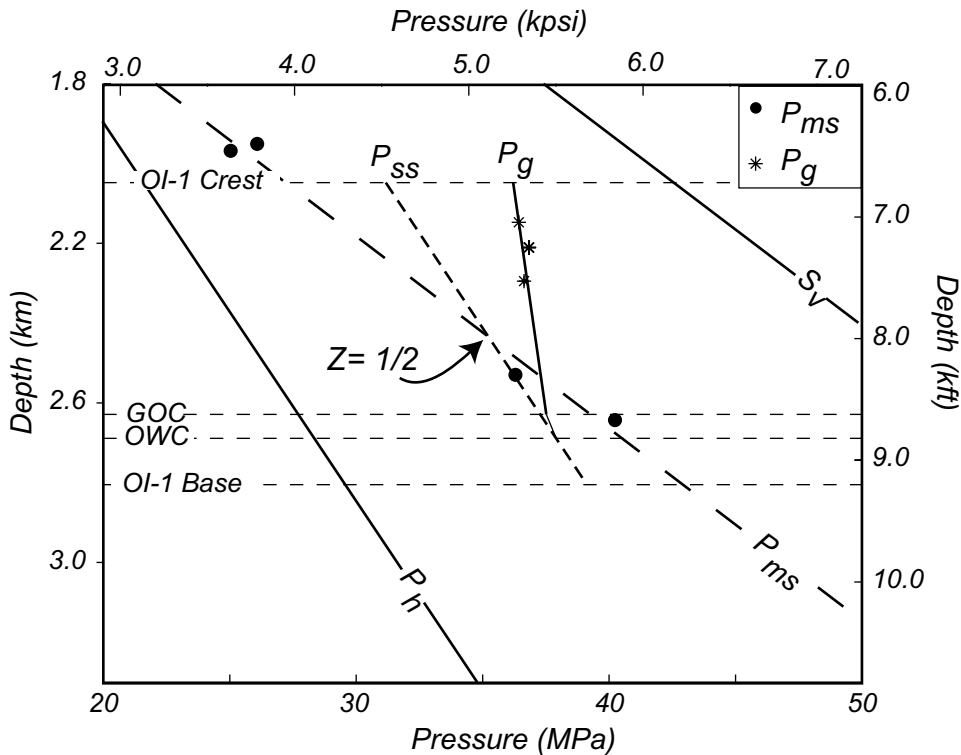


Fig. 12. Pressure-depth plot for the OI-1 FB B. Black circles illustrate porosity-predicted mudstone pressures (P_{ms}) immediately above the OI-1 at four penetrations (table 3). At the crest, the water phase pressure (P_{ss}) and the gas phase pressure (P_g) are significantly greater than P_{ms} . P_{ss} equals P_{ms} in the overlying mudstone at 2500 m (8200 ft) and $Z \sim 1/2$. P_{ms} line is a linear regression of predicted mudstone pressure values (circles). Reservoir pressures are calculated by extrapolating known pressure gradients (table 1) from measured values (stars) in the OI-1 FB-B reservoir.

Unloading can result from burial of a sandstone by overpressured mudstone (fig. 14). In this example, the sandstone body is initially horizontal, and there is steady vertical flow (fig. 14A). Subsequently, the sandstone rotates 45° , and steady flow is re-established. As a consequence of rotation, the effective stress at the crest decreases, and the effective stress at the base increases (fig. 14B). Because elastic deformation is a small component of the total deformation, porosity recovery is small during unloading (open box, fig. 14B). As a result, mudstones at the crest have a lower porosity than would be expected if the unloading had followed the plastic compaction trend.

If equation (9) is applied to predict pressure from this porosity field, the overpressures in figure 14C result. At the crest of the sandstone, porosity-predicted pressure contours are horizontal and the mudstone pressures are less than the *in-situ* mudstone pressures. As a result, there is an apparent jump in pressure from the mudstone pressure to the sandstone pressure (fig. 14D). In contrast, pressures are continuous from sandstone to mudstone at the base of the structure (fig. 14C). Porosity-predicted pressures are thus a lower-bound estimate of the *in-situ* pressure because a decrease in effective stress is not recorded by the mudstone. This behavior may explain the observation that at the crest of the EI-330 reservoirs, pressure contours are sub-horizontal and record pressures less than the *in-situ* pressures in the adjacent sandstones.

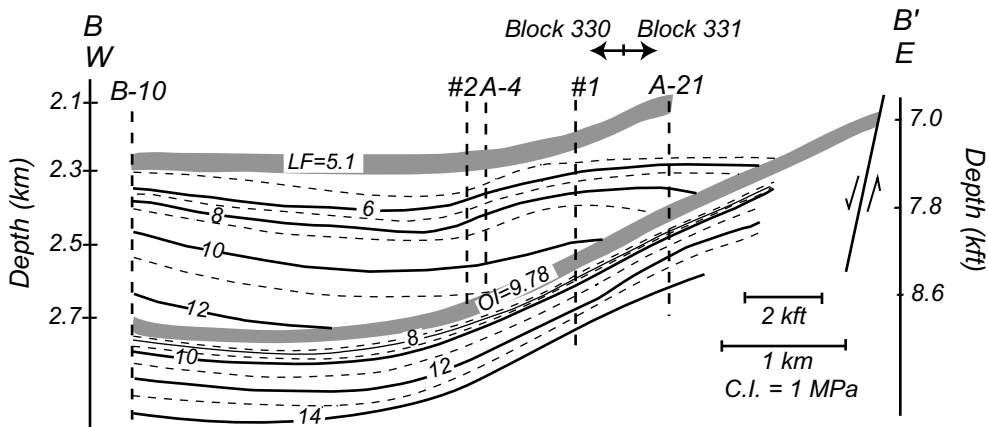


Fig. 13. Overpressure cross-section for mudstone that bounds the OI-1 reservoir (contours in MPa). Vertical dashed lines locate the well penetrations from which the overpressure contours are constructed. The LF and the OI-1 reservoirs are shaded and their reservoir water-phase pressures (P_{ss}) are shown. B-B' is located in figure 11.

Previous studies also interpreted that the difference between porosity-derived mudstone pressures and *in-situ* reservoir pressures results from hysteresis (Scott and Thomsen, 1993; Bowers, 1994; Hart and others, 1995). Bowers (2001) inferred unloading in the A20ST-2 well, which penetrated the OI-1 reservoir in Fault Block E. He suggested that resistivity and velocity respond more dramatically to unloading than does density, and he documented this in mudstones bounding the OI-1.

Hydrodynamic Evolution of the Lentic-1 and OI-1 Sandstones

We combine insights gained from flow modeling, the assumption that the porosity records the maximum effective stress the rock has experienced, and the geological evolution of these reservoirs, to qualitatively predict the evolution of pressure during burial of the Lentic-1 and the OI-1 reservoirs (fig. 15). The Lentic-1 became overpressured at a depth not greater than 1 km (t_2) (the depth where the effective stress at hydrostatic conditions is equal to the effective stress recorded in the mudstones) (fig. 15A and B). It was then buried along the lithostatic stress gradient (fig. 15A and B). Unloading occurred in the crest of the Lentic-1 as rotation occurred (fig. 14). Thus, P_{ms} , the porosity-predicted mudstone pressure, is less than the *in-situ* mudstone pressure at the crest.

One burial history that is compatible with most of the observations in the OI-1, is that it was hydrostatically pressured to a depth not greater than 1.5 km (t_1 to t_2 , fig. 15C and D). During this time, the overpressured mudstone beneath the OI-1 drained into the OI-1 sandstone, and the entire OI-1 drained its fluid to a shallower reservoir or perhaps the seafloor. With further burial ($t_2 - t_3$), the OI-1 became isolated, and its pressure increased along the lithostatic gradient (fig. 15D). This interpretation does not reconcile the observation that P_{ms}^* in the overlying mudstone is greater than beneath the mudstone, which means that at nearly equivalent depths, the mudstone is more compacted below the OI-1 than above it. We are perplexed by this observation; it could result from different mudstone properties above and below the OI-1.

Implications and Applications

We used simple hydrodynamic models and observations of compaction to illuminate the spatial distribution of pressure and flow within a dipping sandstone sur-

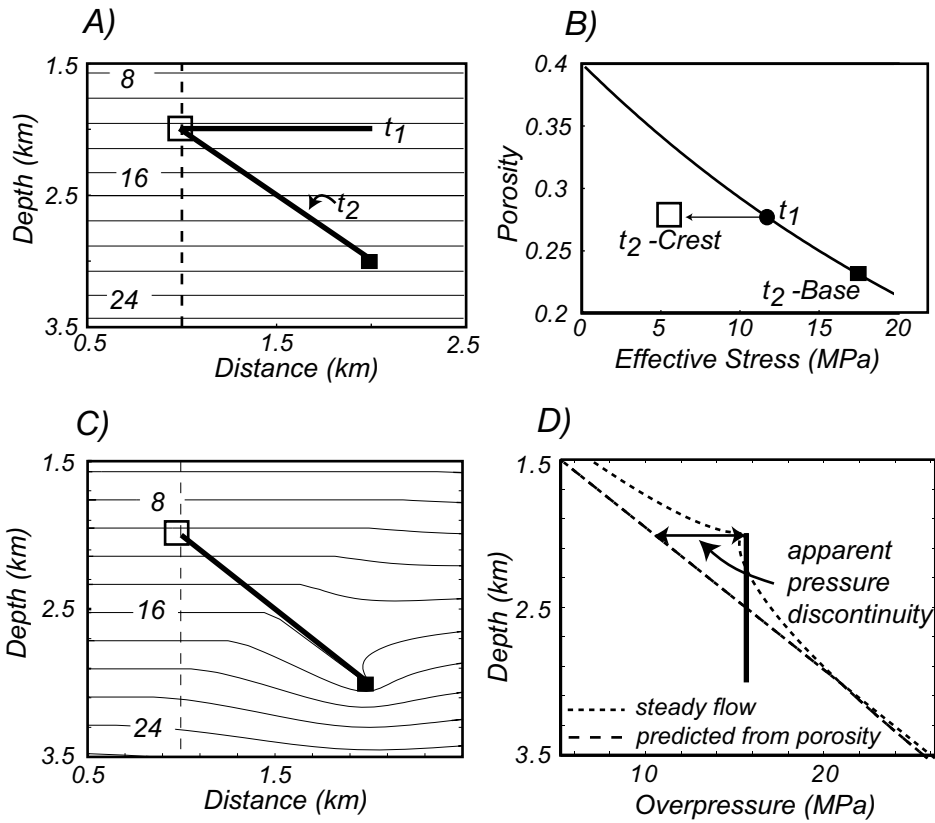


Fig. 14. Simulation of unloading due to sandstone burial and rotation. (A) Sandstone is initially horizontal (t_1), and pressures follow the lithostatic gradient (contours in MPa). Sandstone is rotated 45° (t_2) and steady-flow is established (for example, fig. 3). (B) Porosity versus vertical effective stress. The mudstone is originally at a porosity-effective stress location marked by solid circle. After rotation, the effective stress decreases at the crest, but porosity does not change (open box- t_2 -crest). At the base, the effective stress increases and the mudstone is compacted (solid box- t_2 -base). (C) Overpressure predicted from equation (7) assuming no dilation during unloading. At the crest, overpressure contours are flat, unlike figure 3A. (D) Pressure prediction in a vertical profile through the crest. Unloading generates an apparent pressure discontinuity between the porosity-predicted mudstone pressure and the sandstone pressure. The far field mudstone pressure gradient is $\frac{dS_v}{dz} = 21.0$ MPa/km. P^* equals zero at 1 km depth.

rounded by overpressured mudstone. One fundamental result is that pressures within sandstones follow the hydrostatic gradient, and pressures in bounding mudstones follow steeper, often lithostatic, gradients. A consequence of this behavior is that sandstone pressure converges on the absolute stresses at the crests of structures. This pressure convergence controls hydrocarbon migration, affects well bore stability, and contributes to submarine landslides.

A simple model for stress-controlled hydrocarbon migration is to assume no migration when the hydrocarbon phase pressure is less than the least principle stress in the mudstone, and to assume migration when the hydrocarbon phase pressure equals the least principal stress in the mudstone and hydraulic fracturing occurs. We assume the least principal stress in the mudstone is proportional to pore pressure and overburden stress:

$$S_{\text{hmin}} = K(S_v - P_{ms}) + P_{ms} \quad (10)$$

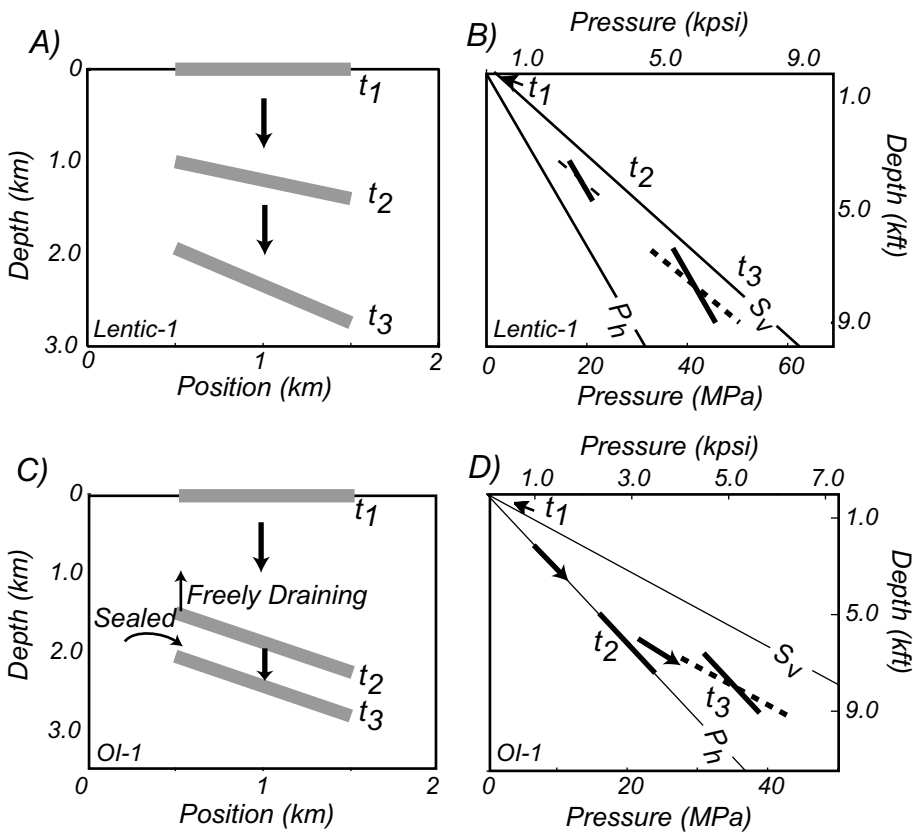


Fig. 15. Evolution of Lentic-1 sandstone (A and B) and OI-1 sandstone (C and D). (A and B) The Lentic-1 sandstone became overpressured at a depth not greater than 1.0 km. Thereafter its pressure increased along the lithostatic gradient and the sandstone rotated to its present position. (C and D) The OI-1 sandstone was buried along the hydrostatic pressure gradient (t_1 - t_2) to a depth of 1.5 km. During further burial its pressure increased along the lithostatic gradient. Thick, solid lines in (B and D) are P_{ss} ; dotted lines in (B and D) are regional P_{ms} .

The least principal stress (S_{hmin}) is horizontal because the maximum principal stress (S_v) is assumed to be vertical, as is commonly found in passive margin basins. K is the effective stress ratio. Equation (10) is derived either from a model where the crust is in a state of brittle failure (Jaeger and Cook, 1979) or a model that assumes elastic crust has deformed uniaxially (Roegiers, 1989). Finkbeiner and others (2001) document K at EI-330.

We use the steady flow model to predict hydrocarbon entrapment in an overpressured synclinal reservoir where the crest of one limb is 1500 meters shallower than the other (fig. 16). At the crest of the shallow structure, P_{ss} is 3 MPa less than S_{hmin} ; as a result, only a 364 meter gas column is trapped before additional hydrocarbons leak vertically (fig. 16). On the deeper limb, P_{ss} is 11.8 MPa less than S_{hmin} and 1506 meters of gas could be trapped. However, because the lower limb only has 1500 meters of relief, the hydrocarbons fill the deeper limb and then migrate from the base of the sand (the synclinal spill point) to the higher structure (fig. 16). Thus, flow focusing within overpressured sandstones controls the amount of hydrocarbons that can be trapped and the migration pathway.

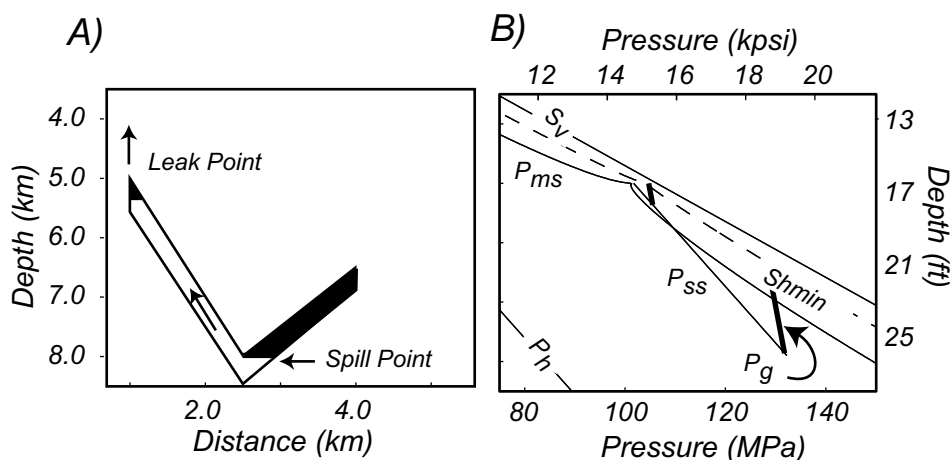


Fig. 16. The effect of flow focusing on hydrocarbon migration in a synclinal reservoir with one shallow limb and one deep limb (A). Gas is shaded black. P_{ss} (water phase pressure) and P_{ms} (mudstone pressure) are calculated from the steady-flow model for a reservoir dipping 60° with 3 km of relief. At the crest of the shallow limb, P_{ss} is very close to S_{hmin} (B), and only a small gas column is trapped. However, at the crest of the lower limb, P_{ss} is much less than S_{hmin} , and a large gas column is trapped. S_{hmin} is calculated from equation (10). $\left(\frac{dP_g}{dz} = 2.26 \text{ MPa/km}, K = 0.6, \frac{dP_h}{dz} = 10.52 \text{ MPa/km}, \frac{dS_v}{dz} = 21.3 \text{ MPa/km}, P_{ss}^* = 49.1 \text{ MPa}\right)$.

We observed this behavior at EI-330. Finkbeiner and others (2001) showed that in the Lentic-1 (fig. 7) and in the OI FB A, D and E reservoirs (fig. 11), the hydrocarbon pressures have converged on the least principal stress and vertical migration is occurring. In contrast, in the OI FB B and C reservoirs, hydrocarbons filled the structure to its spill point before the least principal stress was reached, and hydrocarbons migrated laterally from the down-dip spill point to the west to fill the adjacent structure in the EI-331 field (fig. 11). Finkbeiner and others (2001) showed that the water-phase overpressures are higher in Fault Blocks A, D and E (where small amounts of oil and little gas are trapped) than in Fault Blocks B and C (where a large gas column is trapped). This suggests that the water-phase pressure, which is driven by flow focusing, is a primary control on the magnitude of trapped hydrocarbons.

Others have described the consequences of pore pressures that converge on the least principal stress at the crest of structures. Watts (1987) suggested that hydrocarbons could not be trapped at elevated fluid pressures because hydraulic fracturing resulted. In the North Sea, Gaarenstroom and others (1993) documented small hydrocarbon columns where pore pressures converge on S_{hmin} . Darby and others (1996, 1998) and Illife and others (1999) described how permeable systems with relief create leak-points at the crests of structures. Cosgrove (2001) and Boehm and Moore (2002) documented the presence of sedimentary dikes recording hydraulic fracturing where overpressured and unconsolidated sands have been injected into more cohesive overlying mudstones at the crests of structures.

To drill the crest of the structure in figure 16, a borehole fluid density of 2.1 g/cc must be used in order for the borehole pressure to exceed P_{ss} , the reservoir pressure (fig. 17C). With this fluid density, the borehole pressure will exceed the least principal stress (S_{hmin}) in the mudstone at depths shallower than 4.7 kilometers (fig. 17C). If the borehole is open to the formation in this zone, the drilling fluids will fracture and enter the formation instead of returning to the drill rig. For this reason, casing is periodically set to protect the shallow borehole from the pressures necessary to drill

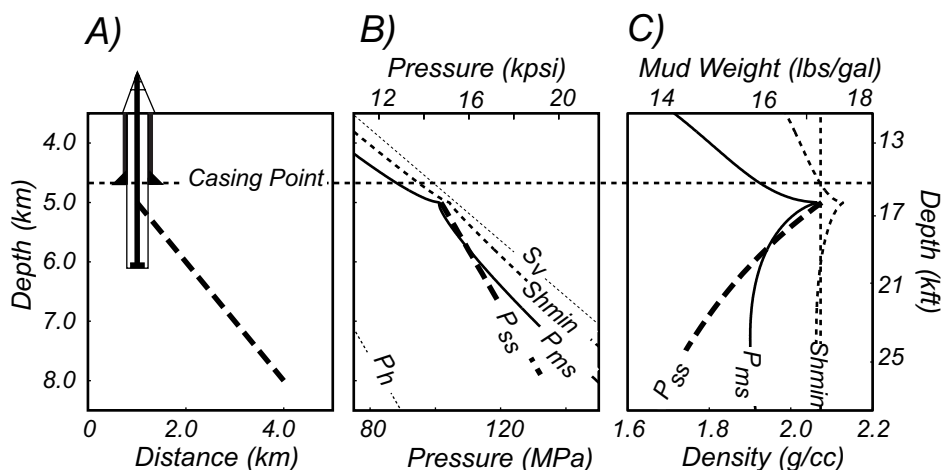


Fig. 17. Pressure and stresses encountered during drilling the shallow limb of fig. 16. (A) Well penetrates crest of sandstone that is dipping 60° with 3 km of relief. (B) Pressure-depth plot. Steady-flow in the sand results in near-lithostatic pressures at the crest. (C) Density (Equivalent Mud Weight)-depth plot. P_{ss} is the borehole fluid density that generates a pressure equal to the sandstone pressure at each depth. P_{ms} is the borehole fluid density that generates a borehole pressure equal to the mudstone pressure along the well bore. S_{hmin} is the borehole fluid density that results in a pressure equal to the least principal stress in the formation along the well bore. Borehole fluid density is often expressed as a mudweight in pounds per gallon. Casing must be set between 4.7 km and the sandstone crest in order to penetrate the sandstone successfully. Parameters defined in caption to figure 16.

the deeper horizons. In this example, casing must be set between 4.7 kilometers and the top of the reservoir at 5.0 kilometers (fig. 17).

Overpressured reservoirs with significant relief increase the number of casing strings that are necessary because pore pressure is close to the least principle stress. Traugott (1997) suggested that one solution is to drill lower on structures where the gap between the pore pressure and the least principal stress is greater. Identical processes cause problems drilling very shallow overpressured sandstone bodies (Byrd and others, 1996; Alberty and others, 1997; Ostermeier and others, 2000; Bruce and others, 2001).

Flow is not necessarily focused towards the crests of sandstone bodies when there is significant seafloor relief. For example, on progradational continental margins, it is common for mudstones to asymmetrically load underlying horizontal sandstones (fig. 18). Sediment loading drives flow laterally along the permeable layer, and low effective stresses are generated at the toe of the slope where the overburden is thin. This process may cause instability on the down slope portions of continental margins even though sedimentation rates are low (Terzaghi, 1950; Dugan and Flemings, 2000, 2002).

Flow focusing in a dipping overpressured sandstone body is analogous to a range of broader geological phenomena. Walther and Orville (1982) described a fracture propagation model where pore fluid pressures within fractures follow the hydrostatic gradient while the bounding stress state is lithostatic. In accretionary prisms, the decollement is commonly assumed to be more permeable than the bounding material (Masche and Moore, 1990; Wuthrich and others, 1990; Bekins and others, 1995). Deep within the prism, flow is driven into the fault plane, flow is then focused laterally along the fault plane, and ultimately where the overburden is thin, pore fluid pressures in the permeable fault exceed the pore pressure in bounding mudstones and converge on the least principle stress. Boulton and others (1995) described how flow is driven downward by the elevated head within the thicker parts of glaciers. Flow is then driven

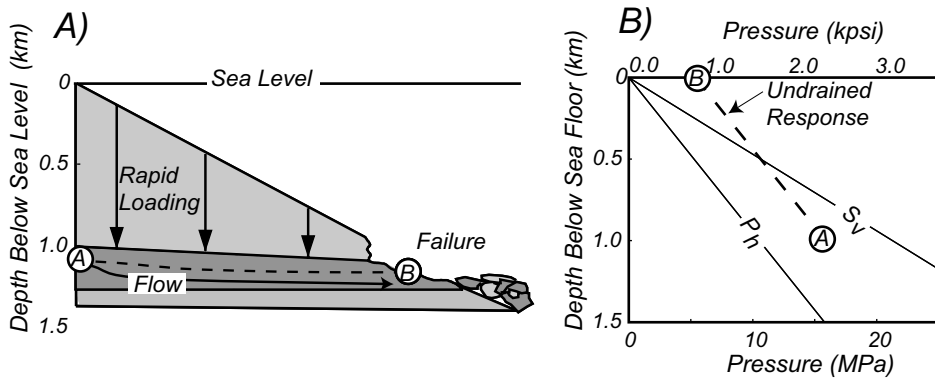


Fig. 18. Rapid sediment-loading at continental margins focuses flow and generates slope instability. (A) A 1 km thick, triangular body of mudstone loads a permeable sandstone and drives flow laterally. (B) Where overburden is thin, pore pressures converge on the overburden stress and slope failure is likely to occur. Dotted line illustrates the undrained response (appendix). $\left(\frac{dP_h}{dz} = 10.52 \text{ MPa/km}, \frac{dS_v}{dz} = 21.3 \text{ MPa/km}\right)$.

laterally underneath the glacier within permeable aquifers towards the toe where it is expelled. They predicted hydraulic fracturing and liquefaction at the toe of the glacier would be recorded in sediment dikes, and they gave examples where this has occurred.

CONCLUSIONS

When a dipping permeable sandstone is encased in overpressured, low permeability mudstone, the pressure gradient within it is hydrostatic, whereas the pressure gradient in the mudstone is greater. This drives a flow system where fluids are drawn in at the base of the sandstone and expelled at the crest. The precise pressure field that develops is dependent on the timescale of formation, the structural geometry, and the reservoir geometry. At the timescales that most geological structures form, even in rapidly formed sedimentary basins, this flow field is well developed.

Geologic history and insights gained from flow modeling are integrated to infer the state and the evolution of pressure and stress in two reservoirs in the Eugene Island 330 field. The Lentic-1 sandstone became overpressured at a shallow depth (1 km); flow is focused in the sandstone and expelled at the crest. The OI-1 sandstone was hydrostatically pressured to a depth of 2 kilometers, and it drained its bounding mudstones. Late in its history, it became overpressured.

Fluid pressures in the crest of overpressured reservoirs converge on the least principal stress. In this situation, permeability will self-generate by hydraulic fracturing or other mechanisms. An understanding of this behavior can be used to predict the migration and trapping of hydrocarbons, drill stable boreholes, and estimate the stability of the continental slope. Overpressured reservoirs are one example of a class of problems where flow focusing drives important geological phenomena. Examples include crack propagation, flow in accretionary prisms, and glacial hydrodynamics.

ACKNOWLEDGMENTS

This research was supported by the Gas Research Institute (Contract #5095-260-3558), the National Science Foundation (Contract #EAR 96-14689), and Penn State's GeoFluids and GeoFluidsII Consortiums (Amerada Hess, Anadarko, BHP, BP, Burlington Resources, ChevronTexaco, Conoco, Devon, ExxonMobil, PanCanadian, Phillips, Shell, and Unocal). Pennzoil, Shell, and Texaco provided the data. M. Maler, A. Huffman, G. Yardley, E. Davis, S. Tennant, B. Dugan, M. Traugott, P. Heppard and G.

Bowers provided insight into the effect of structural relief on fluid pressure. Paradigm's GeologTM software was used. We thank the Associate Editor, and anonymous reviewers for insightful comments that have strengthened this work.

APPENDIX

Undrained Model

When a sediment volume is buried by a thickness of rock dz , the increase in overburden stress is,

$$dS_v = \rho_b g dz. \quad (11)$$

If the rock is undrained, equation (1) yields,

$$DP = B \rho_b g dz. \quad (12)$$

B , the pore pressure build-up coefficient ($B = \frac{\beta}{\beta + \beta_f(1 - \phi)}$) equals ~ 0.99 at E.I 330 ($\beta = 3.13 \times 10^{-2}$ MPa⁻¹, (eq 7, fig. 7), $\phi = 0.3$, $\beta_f = 4.88 \times 10^{-4}$ MPa⁻¹).

A sandstone body of variable thickness $dh(x, y)$ and volume V_{ss} is buried by mudstone of variable thickness $dz(x, y)$. The volume integral of equation (1) is,

$$\int_V \left(\frac{\beta \phi}{(1 - \phi)} + \phi \beta_f \right) \left(\frac{DP_{ss}}{Dt} \right) DV_{ss} = \int_V \frac{1}{\rho_f} \left(\nabla \cdot \frac{k \rho_f}{\mu} \nabla P^* \right) DV_{ss} + \int_V \frac{\beta \phi}{(1 - \phi)} \left(\frac{DS_v}{Dt} \right) DV_{ss}. \quad (13)$$

There is no flow into or out of the sandstone; thus the second term is zero. Within the permeable sandstone, flow equilibrates the pressure to the hydrostatic gradient. Therefore, sandstone overpressure (DP_{ss}^*) is,

$$DP_{ss}^* = DP_{ss} - \rho_f g dz(x, y). \quad (14)$$

Equations (12), (13), and (14) are combined to determine DP_{ss}^* .

$$DP_{ss}^* = (B \rho_b - \rho_f) g \frac{\int_V dz(x, y) DV_{ss}}{V_{ss}}. \quad (15)$$

Equation (15) is solved for several geometries below.

2D: planar reservoir (figs. 1 and 2A).—A sandstone body of length l has a trapezoidal shape ($dh(x) = C_3 + C_4 x$), and it is buried by a trapezoidal load ($dz(x) = C_1 + C_2 x$). The sandstone overpressure is,

$$DP_{ss}^* = (B \rho_b - \rho_f) g \frac{\left(C_1 C_3 l + \frac{(C_2 C_3 + C_4 C_1) l^2}{2} + \frac{C_2 C_4 l^3}{3} \right)}{C_3 l + \frac{C_4 l^2}{2}}. \quad (16)$$

If the sandstone is of constant thickness ($C_4 = 0$), its pressure equals the mudstone pressure at the structural midpoint of the sandstone ($Z = 1/2$) (fig. 1). A triangular sandstone that thickens downdip has its pressures equal to the mudstone pressure one third of the way down from the top of the structure ($Z = 1/3$) (fig. 2A).

2D: anticlines and synclines (fig. 3B).—If the load geometry is parabolic ($z(x) = -\frac{x^2}{4P}$) and the sandstone thickness is constant, then

$$DP_{ss}^* = (B \rho_b - \rho_f) g \frac{l}{3}. \quad (17)$$

3D: domes and bowls (fig. 3C).—In radial coordinates, equation (15) can be re-stated as,

$$DP_{ss}^* = (B\rho_b - \rho_f)g \frac{\int_{\theta=0}^{\theta=2\pi} \int_{r=0}^{r=l} dz(r, \theta) r dr d\theta}{V_{ss}}. \quad (18)$$

This result is illustrated in figure 2C for a cone-shaped structure.

Steady Flow Model

Phillips (1991) followed Lamb (1932) and solved for flow through a low permeability medium surrounding a permeable lens. He used an elliptical coordinate system such that x and z are functions of ξ , η , and a .

$$x = a \cosh \xi \cos \eta \quad (19)$$

$$z = a \sinh \xi \sin \eta \quad (20)$$

Lines of constant ξ form ellipses, lines of constant η are hyperbolae, a is the half-length of the sandstone, and γ is the angle between the undisturbed flow velocity and the sandstone. The stream function (Ψ) is calculated as a function of the transformed coordinates, a , and U (far field flow velocity),

$$\Psi = Ua \cosh \xi \sin(\eta - \gamma). \quad (21)$$

The flow potential (Φ) is,

$$\Phi = Ua \sinh \xi \cos(\eta - \gamma) \quad (22)$$

The flow velocity at any location is calculated by taking the derivative of the stream function, and the pressure gradient is calculated from Darcy's law. Stump (ms, 1998) presented a detailed analysis of this approach.

REFERENCES

- Alberty, M. W., Hafle, M. E., Minge, J. C., and Byrd, T. M., 1997, Mechanisms of shallow waterflows and drilling practices for intervention, Proceedings of the 29th Annual Offshore Technology Conference: Dallas, Texas, p. 241–247.
- Alexander, L. L., and Flemings, P. B., 1995, Geologic Evolution of a Pliocene-Pleistocene Salt-Withdrawal Minibasin: Eugene Island Block 330, Offshore Louisiana: AAPG Bulletin, v. 79, p. 1737–1756.
- Athy, L. F., 1930, Density, Porosity, and Compaction of Sedimentary Rocks: American Association of Petroleum Geologist Bulletin, v. 14, p. 1–24.
- Becker, K., Fisher, A. T., and Davis, E. E., 1997, The CORK Experiment in Hole 949C: long-term observations of pressure and temperature in the Barbados accretionary prism, in Miller, C. M., editor, Proceedings of the Ocean Drilling Program, Scientific Results: College Station, TX, Texas A & M University, Ocean Drilling Program, p. 247–252.
- Bekins, B. A., Dreiss, S., and McCaffrey, A. M., 1995, Episodic and Constant Flow Models for the Origin of Low-Chloride Waters in a Modern Accretionary Complex: Water Resources Research, v. 31, p. 3205–3215.
- Bethke, C. M., 1985, A Numerical Model of Compaction-Driven Groundwater Flow and Heat Transfer and Its Application to the Paleohydrology of Intracratonic Sedimentary Basins: Journal of Geophysical Research, v. 90, p. 6817–6828.
- Biot, M. A., 1941, General Theory of Three-Dimensional Consolidation: Journal of Applied Physics, v. 12, p. 155–164.
- Boatman, W. A., 1967, Measuring and using shale density to aid in drilling wells in high-pressure areas: Journal of Petroleum Technology, v. 19, p. 1423–1429.
- Boehm, A., and Moore, J. C., 2002, Fluidized sandstone intrusions as an indicator of paleostress orientation, Santa Cruz, California: Geofluids, v. 2, p. 147–161.
- Boulton, G. S., Caban, P. E., and Van Gijssel, K., 1995, Groundwater Flow Beneath Ice Sheets: Part I - Large Scale Patterns: Quaternary Science Reviews, v. 14, p. 542–562.
- Bowers, G. L., 1994, Pore pressure estimation from velocity data: Accounting for overpressure mechanisms besides undercompaction: Society of Petroleum Engineers, SPE 27488, p. 515–529.
- 2001, Determining an appropriate pore-pressure estimation strategy, Offshore Technology Conference: Houston, Texas, OTC 13103, 14 p.
- Bruce, B., Bowers, G., and Borel, R., 2001, Well planning for shallow water flows and overpressures-The Kestrel Well, Offshore Technology Conference: OTC 13104, 10 p.

- Byrd, T. M., Schneider, J. M., Reynolds, D. J., Alberty, M. W., and Hafle, M. E., 1996, Identification of "flowing water sand" drilling hazards in the deepwater Gulf of Mexico: Dallas, Proceedings of the 28th annual Offshore Technology Conference, p. 137–146.
- Cosgrove, J. W., 2001, Hydraulic fracturing during the formation and deformation of a basin: A factor in the dewatering of low-permeability sediments: American Association of Petroleum Geologists Bulletin, v. 85, p. 737–748.
- Crawford, C. B., 1986, State of the art; evaluation and interpretation of soil consolidation tests, *in* Yong, R. N., and Townsend, F. C., editors, Consolidation of soils; testing and evaluation: Philadelphia, American Society for Testing and Materials, STP 892, p. 71–103.
- Darby, D., Haszeldine, R. S., and Couples, G. D., 1996, Pressure cells and pressure seals in the UK Central Graben: Marine and Petroleum Geology, v. 13, p. 865–878.
- 1998, Central North Sea overpressures: insights into fluid flow from one- and two-dimensional basin modelling, *in* Duppenbecker, S. J., and Iliffe, J. E., editors, Basin Modelling: Practice and Progress: London, Geological Society Special Publications, no. 141, p. 95–107.
- Dickinson, G., 1953, Geological aspects of abnormal reservoir pressures in Gulf Coast Louisiana: American Association of Petroleum Geologists Bulletin, v. 37, p. 410–432.
- Dugan, B., and Flemings, P. B., 2000, Overpressure and Fluid Flow in the New Jersey Continental Slope: Implications for Slope Failure and Cold Seeps: Science, v. 289, p. 288–291.
- 2002, Fluid flow and stability of the US continental slope offshore New Jersey from the Pleistocene to the present: Geofluids, v. 2, p. 137–146.
- Eaton, B. A., 1975, The equation for geopressure prediction from well logs, Fall meeting of the Society of Petroleum Engineers: Dallas, Texas, SPE 5544, 11 p.
- England, W. A., Mackenzie, A. S., Mann, D. M., and Quigley, T. M., 1987, The movement and entrapment of petroleum fluids in the subsurface: Journal of the Geological Society of London, v. 144, p. 327–347.
- Finkbeiner, T., Stump, B. B., Zoback, M. D., and Flemings, P. B., 1996, Pressure (Pp), overburden (Sv), and minimum horizontal stress (Shmin) in Eugene Island Block 330, offshore Gulf of Mexico: Gas Research Institute, report GRI-96/0285, 16 p.
- Finkbeiner, T., Zoback, M., Stump, B. B., and Flemings, P. B., 2001, Stress, Pore Pressure, and Dynamically Constrained Hydrocarbon Columns in the South Eugene Island 330 Field, Gulf of Mexico: American Association of Petroleum Geologists Bulletin, v. 85, p. 1007–1031.
- Gaarenstroom, L., Tromp, R. A. J., de Jong, M. C., and Brandenburg, A. M., 1993, Overpressures in the Central North Sea: implications for trap integrity and drilling safety, Petroleum Geology of Northwest Europe: London, United Kingdom, The Geological Society, 4th Conference, p. 1305–1313.
- Gibson, R. E., 1958, The progress of consolidation in a clay layer increasing in thickness with time: Geotechnique, v. 8, p. 171–182.
- Gordon, D. S., and Flemings, P. B., 1998, Generation of overpressure and compaction-driven fluid flow in a Plio-Pleistocene growth-faulted basin, Eugene Island 330, offshore Louisiana: Basin Research, v. 10, p. 177–196.
- Green, D. H., and Wang, H. F., 1986, Fluid pressure response to undrained compression in saturated sedimentary rock: Geophysics, v. 51, p. 948–956.
- Ham, H. H., 1966, A method of estimating formation pressures from Gulf Coast well logs: Transactions - Gulf Coast Association of Geological Societies, v. 16, p. 185–197.
- Harrison, W. J., and Summa, L. L., 1991, Paleohydrology of the Gulf of Mexico Basin: American Journal of Science, v. 291, p. 109–176.
- Hart, B. S., Flemings, P. B., and Deshpande, A., 1995, Porosity and pressure: Role of compaction disequilibrium in the development of geopressures in a Gulf Coast Pleistocene basin: Geology, v. 23, p. 45–48.
- Holland, D. S., Nunan, W. E., and Lammlin, D. R., 1990, Eugene Island Block 330 field - U.S.A., offshore Louisiana, *in* Foster, N. H., and Beaumont, E. A., editors, Structural Traps III, Tectonic fold and fault traps: Treatise of petroleum geology, Atlas of oil and gas fields: Tulsa, Oklahoma, American Association of Petroleum Geologists, p. 103–143.
- Hottman, C. E., and Johnson, R. K., 1965, Estimation of formation pressures from log-derived shale properties: Journal of Petroleum Technology, v. 17, p. 717–722.
- Iliffe, J. E., Robertson, A. G., Wynn, G. H. F., Pead, S. D. M., and Cameron, N., 1999, The importance of fluid pressures and migration to the hydrocarbon prospectivity of the Faeroe-Shetland White Zone, *in* Fleet, A. J., and Boldy, S. A. R., editors, Petroleum Geology of Northwest Europe: Proceedings of the 5th Conference: London, Geological Society, p. 601–611.
- Issler, D. R., 1992, A new approach to shale compaction and stratigraphic restoration, Beaufort- Mackenzie Basin and Mackenzie Corridor, northern Canada: American Association of Petroleum Geologist Bulletin, v. 76, p. 1170–1189.
- Jaeger, J. C., and Cook, N. G. W., 1979, Fundamentals of rock mechanics: Science Paperbacks v. 18: New York, Chapman and Hall, 593 p.
- Karig, D. E., and Hou, G., 1992, High-stress consolidation experiments and their geologic implications: Journal of Geophysical Research, v. 97, p. 289–300.
- Lamb, H., 1932, Hydrodynamics: Cambridge, The University Press, 738 p.
- MacGregor, J. R., 1965, Quantitative determination of reservoir pressures from conductivity log: American Association of Petroleum Geologists Bulletin, v. 49, p. 1502–1511.
- Mann, D. M., and Mackenzie, A. S., 1990, Prediction of pore fluid pressures in sedimentary basins: Marine and Petroleum Geology, v. 7, p. 55–65.
- Masle, A., and Moore, J. C., 1990, ODP Leg 110; tectonic and hydrologic synthesis, *in* Winkler, W. R., editor, Proceedings of the Ocean Drilling Program, Scientific Results: College Station, TX, Texas A & M University, Ocean Drilling Program, p. 409–422.

- Moore, J. C., and Tobin, H. J., 1997, Estimated fluid pressures of the Barbados accretionary prism and adjacent sediments in Miller, C. M., editor, Proceedings of the Ocean Drilling Program, Scientific Results: College Station, TX, Texas A & M University, Ocean Drilling Program, p. 229–238.
- Moore, J. C., Shipley, T. H., Goldberg, D., Ogawa, Y., Filice, F., Fisher, A., Jurado, M. J., Moore, G. F., Rabaute, A., Yin, H., Zwart, G., Brueckmann, W., Henry, P., Ashi, J., Blum, P., Meyer, A., Housen, B., Kastner, M., Labaume, P., Laier, T., Leitch, E. C., Maltman, A. J., Peacock, S., Steiger, T. H., Tobin, H. J., Underwood, M. B., Xu, Y., and Zheng, Y., 1995, Abnormal fluid pressures and fault-zone dilation in the Barbados accretionary prism; evidence from logging while drilling: *Geology*, v. 23, p. 605–608.
- Neuzil, C. E., 1993, Low fluid pressure within the Pierre Shale; a transient response to erosion: *Water Resources Research*, v. 29, p. 2007–2020.
- 1994, How permeable are clays and shales?: *Water Resources Research*, v. 30, p. 145–150.
- 1995, Abnormal pressures as hydrodynamic phenomena: *American Journal of Science*, v. 295, p. 742–786.
- Ostermeier, R. M., Pelletier, J. H., Winker, C. D., Nicholson, J. W., Rambow, F. H., and Cowan, K. M., 2000, Dealing with Shallow-Water Flow in the Deepwater Gulf of Mexico, Offshore Technology Conference 2000: Houston, Texas, OTC 11972.
- Ostermeier, R. M., Pelletier, J. H., Winker, C. D., and Nicholson, J. W., 2001, Trends in Shallow Sediment Pore Pressures - Deepwater Gulf of Mexico: Society of Petroleum Engineers, v. SPE/IADC 67772.
- Palciauskas, V. V., and Domenico, P. A., 1989, Fluid pressures in deforming porous rocks: *Water Resources Research*, v. 25, p. 203–213.
- Pennebaker, E. S., 1968, Seismic data indicate depth, magnitude of abnormal pressure: *World Oil*, v. 166, p. 73–78.
- Pestana, J. M., and Whittle, A. J., 1999, Formulation of a Unified Constitutive Model for Clays and Sands: *International Journal for Numerical and Analytical Methods in Geomechanics*, v. 23, p. 1215–1243.
- Phillips, O. M., 1991, Flow and reactions in permeable rocks: New York, Cambridge University Press, 285 p.
- Raiga-Clemenceau, J., Martin, J. P., and Nicoletis, S., 1986, The concept of acoustic formation factor for more accurate porosity determination from sonic transmit time data, Transactions of the SPWLA twenty-seventh annual logging symposium: Houston, Society of Professional Well Log Analysts, p. G1–G14.
- Raymer, L. L., Hunt, E. R., and Gardner, J. S., 1980, An improved sonic transit time-to-porosity transform, Transactions of the SPWLA twenty-first annual logging symposium: Houston, Society of Professional Well Log Analysts, p. P1–P13.
- Rice, J. A., and Cleary, M. P., 1976, Some basic stress diffusion solutions for fluid-saturated elastic porous media with compressible constituents: *Reviews of Geophysics and Space Physics*, v. 14, p. 227–241.
- Roegiers, J.-C., 1989, Elements of Rock Mechanics, in Economides, M. J., and Nolte, K. G., editors, Reservoir stimulation: Englewood Cliffs, New Jersey, Prentice Hall, p. 2-1–2-22.
- Rowan, M. G., Hart, B. S., Nelson, S., Flemings, P. B., and Trudgill, B. D., 1998, Three-dimensional geometry and evolution of a salt-related growth-fault array; Eugene Island 330 Field, offshore Louisiana, Gulf of Mexico: *Marine and Petroleum Geology*, v. 15, p. 309–328.
- Rubey, W. W., and Hubbert, M. K., 1959, Overthrust belt in geosynclinal area of western Wyoming in light of fluid-pressure hypothesis, [Part] 2 of Role of fluid pressure in mechanics of overthrust faulting: *GSA Bulletin*, v. 70, p. 167–205.
- Schultheiss, P. J., and McPhail, S. D., 1986, Direct indication of pore-water advection from pore pressure measurements in Madeira abyssal plain sediments: *Nature*, v. 320, p. 348–350.
- Scott, D., and Thomsen, L. A., 1993, A global algorithm for pore pressure prediction, Proceedings, 8th Middle East oil show and conference: Society of Petroleum Engineers and the American Institute of Mining, Metallurgical, and Petroleum Engineers (AIME), SPE 25674, p. 645–654.
- Skempton, A. W., 1954, The Pore-Pressure Coefficients A and B: *Geotechnique*, v. 4, p. 143–147.
- Stump, B. B., ms, 1998, Illuminating basinal fluid flow in Eugene Island 330 (Gulf of Mexico) through *in situ* observations, deformation experiments, and hydrodynamic modeling: Masters thesis, The Pennsylvania State University, University Park, 121 p.
- Stump, B. B., and Flemings, P. B., 2002, Consolidation State, Permeability, and Stress Ratio as Determined from Uniaxial Strain Experiments on Mud Samples from the Eugene Island 330 Area, Offshore Louisiana, in Huffman, A. R., and Bowers, G. L., editors, Pressure regimes in sedimentary basins and their prediction: AAPG Memoir 76, p. 131–144.
- Terzaghi, K., 1943, *Theoretical Soil Mechanics*: London, Chapman and Hall, 510 p.
- 1950, Mechanism of landslides, Application of geology to engineering practice: Berkeley volume: New York, Geological Society of America, p. 83–123.
- Traugott, M. O., 1997, Pore/fracture pressure determinations in deep water: *Deepwater Technology* (supplement to *World Oil*), p. 68–70.
- Urgeles, R., Canals, M., Roberts, J., and Party, S. L. P. S., 2000, Fluid flow from pore pressure measurements off La Palma, Canary Islands: *Journal of Volcanology and Geothermal Research*, v. 101, p. 253–271.
- van der Kamp, G., and Gale, J. E., 1983, Theory of Earth tide and barometric effects in porous formations with compressible grains: *Water Resources Research*, v. 19, p. 538–544.
- Wallace, W. E., 1965, Abnormal surface pressure measurements from conductivity or resistivity logs: *Oil & Gas Journal*, v. 63, p. 102–106.
- Walther, J. V., and Orville, P. M., 1982, Volatile production and transport in regional metamorphism: *Contributions to Mineralogy and Petrology*, v. 79, p. 252–257.

- Wang, K., and Davis, E. E., 1996, Theory for the propagation of tidally induced pore pressure variations in layered subseafloor formations: *Journal of Geophysical Research*, v. 101, p. 11,483–11,495.
- Watts, N. L., 1987, Theoretical aspects of cap-rock and fault seals for single- and two-phase hydrocarbon columns: *Marine and Petroleum Geology*, v. 4, p. 274–307.
- Weakley, R. R., 1989, Use of surface seismic data to predict formation pore pressures (sand shale depositional environments), *Drilling Conference, Society of Petroleum Engineers: New Orleans, Louisiana, SPE 18713*, p. 791–806.
- Whittle, A. J., Sutabutr, T., Germaine, J. T., and Varney, A., 2001, Prediction and interpretation of pore pressure dissipation for a tapered piezoprobe: *Geotechnique*, v. 51, p. 601–617.
- Wuthrich, D. R., Screaton, E. J., and Dreiss, S. J., 1990, Fluid flow within the Barbados Ridge complex; Part II, Permeability estimates and numerical simulations of flow velocities and pore pressures: *Proceedings of the Ocean Drilling Program, Scientific Results*, v. 110, p. 331–341.
- Yardley, G. S., and Swarbrick, R. E., 2000, Lateral transfer; a source of additional overpressure?: *Marine and Petroleum Geology*, v. 17, p. 523–537.